NASA TECHNICAL MEMORANDUM

NASA TM X-3365

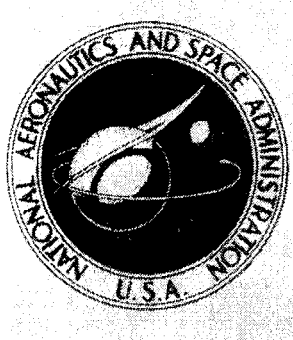

NASA TM X-3365

ANALYSIS OF EXPERIMENTAL RESULTS OF THE INLET FOR THE NASA HYPERSONIC RESEARCH ENGINE AEROTHERMODYNAMIC INTEGRATION MODEL

Earl H. Andrews, Jr., and Ernest A. Mackley

Langley Research Center
Hampton, Va. 23665

NATIONAL AERONAUTICS AND SPACE ADMINISTRATION • WASHINGTON, D. C. • JUNE 1976

1. Report No.	2. Government Accession No.	3. Recipient's Catalog No.
NASA TM X-3365		

4. Title and Subtitle	5. Report Date
ANALYSIS OF EXPERIMENTAL RESULTS OF THE INLET FOR THE NASA HYPERSONIC RESEARCH ENGINE AEROTHERMODYNAMIC INTEGRATION MODEL	June 1976
	6. Performing Organization Code
7. Author(s)	8. Performing Organization Report No.
Earl H. Andrews, Jr., and Ernest A. Mackley	L-10400
	10. Work Unit No.
9. Performing Organization Name and Address	505-05-41-01
NASA Langley Research Center Hampton, Va. 23665	11. Contract or Grant No.
	13. Type of Report and Period Covered
12. Sponsoring Agency Name and Address	Technical Memorandum
National Aeronautics and Space Administration Washington, D.C. 20546	14. Sponsoring Agency Code

15. Supplementary Notes

16. Abstract

An aerodynamic inlet analysis has been performed on the experimental results obtained at nominal Mach numbers of 5, 6, and 7 from the NASA Hypersonic Research Engine (HRE) Aerothermodynamic Integration Model (AIM). Incorporation on the AIM of the mixed-compression inlet design represented the final phase of an inlet development program of the HRE Project. The purpose of this analysis was to compare the AIM inlet experimental results with theoretical results. Experimental performance was based on measured surface pressures used in a one-dimensional force-momentum theorem.

Results of the analysis indicated that surface static-pressure measurements agreed reasonably well with theoretical predictions except in the regions where the theory predicts large pressure discontinuities. Experimental and theoretical results both based on the one-dimensional force-momentum theorem yielded inlet performance parameters as functions of Mach number that exhibited reasonable agreement. Previous predictions of inlet unstart that resulted from pressure disturbances created by fuel injection and combustion appeared to be pessimistic.

17. Key Words (Suggested by Author(s))	18. Distribution Statement
Inlet Propulsion	Unclassified – Unlimited Subject Category 07

19. Security Classif. (of this report)	20. Security Classif. (of this page)	21. No. of Pages	22. Price*
Unclassified	Unclassified	49	$3.75

*For sale by the National Technical Information Service, Springfield, Virginia 22161

ANALYSES OF EXPERIMENTAL RESULTS OF THE INLET FOR THE NASA HYPERSONIC RESEARCH ENGINE AEROTHERMODYNAMIC INTEGRATION MODEL

Earl H. Andrews, Jr., and Ernest A. Mackley
Langley Research Center

SUMMARY

An inlet analysis and a comparison with experiment have been made in support of the aerothermodynamic research program for the NASA Hypersonic Research Engine (HRE) Project. The project culminated in an experimental investigation of the Aerothermodynamic Integration Model (AIM) conducted at nominal Mach numbers of 5, 6, and 7 in the Lewis Hypersonic tunnel facility at the Plum Brook Station. The tests were completed in April 1974. The objective of this investigation was to determine the overall engine performance and aerothermodynamic interaction effects of the inlet, combustor, and nozzle components. This report presents inlet performance computed by using experimental surface-pressure measurements in a one-dimensional force-momentum theorem, and the results are compared with theoretical results, including those based on the same theorem.

The AIM experimental surface-pressure measurements agreed well with theoretical predictions except in regions of shock/boundary-layer interactions. The inlet interacted with the combustor in that the inlet internal shock waves continued into the diverging combustor with an associated total-pressure loss. Stable inlet-combustor operation was achieved over a wide range of fuel equivalence ratio. Although previous predictions of inlet unstart because of pressure disturbances that resulted from fuel injection and combustion were found to be pessimistic, inlet unstart could be initiated only by rapid or excessive fuel injection.

Experimental AIM inlet total-pressure recoveries derived from the force-momentum theorem, when compared with theoretical results based on the same theorem, were up to 10 percent lower at Mach 5 and 6 and 28 percent higher at Mach 7 (where the stream temperature simulates Mach 6). The AIM experimental total-pressure recoveries at an angle of attack of 3° are 87, 68, and 67 percent of the values at an angle of attack of 0° for Mach 5, 6, and 7, respectively.

INTRODUCTION

As part of the NASA Hypersonic Research Engine (HRE) Project, an experimental investigation of a complete engine (inlet, combustor, and nozzle), designated the Aerothermodynamic Integration Model (AIM), was performed. The AIM is a full-scale, water-cooled, boilerplate engine which burns hydrogen fuel. This investigation (completed in April 1974) was conducted at the Lewis Hypersonic tunnel facility at the Plum Brook Station at nominal Mach numbers of 5, 6, and 7 to determine the aerothermodynamic interaction effects of the major components of a complete full-scale engine.

The tunnel stream conditions for the HRE-AIM tests simulated altitudes of 21.6 km (71 000 ft) and 23.5 km (77 000 ft) at Mach numbers of 5 and 6, respectively. The conditions provided full-flight simulation within 0.5 km (1650 ft) of the HRE design Mach-number—altitude profile. (See ref. 1.) At a Mach number of 7 the simulated pressure altitude was 30.8 km (101 000 ft), or about 4.6 km (15 000 ft) above the design Mach-number—altitude profile, because an engine design limitation restricted the maximum free-stream total pressure to 68 atm (facility limit, 80 atm). The total temperature for Mach 7 tests was limited by facility heater deterioration to a Mach 6 simulation at 1695 K (3050° R).

The AIM tests represent the final phase of an inlet development program that was initiated in the early part of the HRE Project. Initially, 1/3- and 2/3-scale inlet models were tested, and the results were compared with theory. (See refs. 2 to 4.) The 2/3-scale inlet model tests yielded satisfactory correlations between the predictions and the experimental results; therefore, the inlet design, referred to as the "T" model inlet in reference 2, was incorporated in the AIM.

The purpose of the present report is to compare the AIM inlet experimental results with theoretical results of reference 1. Results of this analysis are presented in terms of surface-pressure distributions compared with theoretical distributions and correlated with internal-flow shock patterns, inlet-combustor interaction characteristics, and performance parameters that include total-pressure recoveries, throat Mach numbers, and kinetic energy efficiencies.

SYMBOLS

Values are given in both the International System of Units (SI) and U.S. Customary Units. Measurements and calculations were made in U.S. Customary Units.

A area, m^2 (ft^2)

$\frac{A_C}{A_{th}}$ geometric contraction ratio

$\left(\frac{A_C}{A_{th}}\right)\left(\frac{\dot{m}}{\dot{m}_\infty}\right)$ aerodynamic contraction ratio

C_D drag coefficient, $\frac{D}{q_\infty A_C}$

$C_{D,A}$ additive drag coefficient, $\frac{p - p_\infty}{q_\infty A_C}\left[A_C\left(1 - \frac{\dot{m}}{\dot{m}_\infty}\right)\right]$

C_f friction coefficient, $\frac{2\tau_w}{\rho_\delta u_\delta^2}$

D drag, N (lbf)

d fuel injector orifice diameter, cm (in.)

F force, N (lbf)

h enthalpy, J/kg (Btu/lbm)

h' throat height (inclined 95.645° to AIM center line), cm (in.)

M Mach number

$\dot{m}$ captured mass flow, kg/sec (lbm/sec)

$\frac{\dot{m}}{\dot{m}_\infty}$ ratio of captured mass flow to that free-stream mass flow that passes through an area equal to the projected cowl area $\left(\pi R_C^2 = \pi(22.934 \text{ cm})^2 = \pi(9.029 \text{ in.})^2\right)$

N_{Re} Reynolds number based on cowl diameter (diameter equals $2R_{CL}$)

p pressure, atm (psia) (1 atm = 14.69 psia = 0.1013 MN/m^2)

q dynamic pressure, atm (psf) (1 atm = 2117 psf = 0.1013 MN/m^2)

R_C, R_{CL} radii defined in figure 2(c)

R radius nondimensionalized by R_{CL} (R_{CL} = 22.86 cm (9.00 in.), see fig. 2(c))

s fuel injector peripheral separation distance (center-to-center), cm (in.)

T temperature, K (°R)

u	local velocity parallel to surface, m/sec (ft/sec)
V	velocity, m/sec (ft/sec)
X	distance from spike vertex nondimensionalized by R_{CL} (see fig. 2(c))
α	angle of attack, deg
δ	boundary-layer thickness, cm (in.)
δ^*	boundary-layer displacement thickness, cm (in.)
η_{KE}	inlet kinetic energy efficiency
η_R	inlet total-pressure recovery
θ	radial angle, deg (see table II(c))
ξ	wall surface angle, deg
ρ	density, kg/m^3 (lbm/ft^3)
τ_w	wall shear, N/m^2 (lbf/ft^2)
ϕ	fuel-to-air ratio (value of unity is for stoichiometric combustion)

Subscripts:

C	most forward point on cowl lip (see fig. 2(c))
CL	12^o tangent point on cowl lip (see fig. 2(c))
l	local conditions
lip	frontal projection of the cowl blunted lip
t	total or stagnation condition
th	inlet throat

tip	frontal projection of spike blunted tip
tot	accumulative total
δ	boundary-layer-edge values
1	first-stage fuel injectors
∞	free-stream conditions

Abbreviations:

AIM	Aerothermodynamic Integration Model
HRE	Hypersonic Research Engine
HTF	Hypersonic tunnel facility
L.E.	leading edge

APPARATUS AND TESTS

Facility and Tests

Facility.- Experimental tests of the HRE-AIM were conducted in the Lewis Hypersonic tunnel facility (HTF) at the Plum Brook Station at nominal Mach numbers of 5, 6, and 7. A schematic layout of the HTF is shown in figure 1(a). During the tests the AIM was enshrouded, as shown in figure 1(b), with a 28-cm (11-in.) gap between the facility nozzle exit and the ring on the front of the shroud. This test configuration was suggested by results of a subscale tunnel starting investigation reported in reference 5. A thorough description of the HTF and the results of calibration tests are presented in reference 6. Unpublished calibration results yielded free-stream Mach number as a function of total temperature for the Mach 6 and 7 nozzles and were used in determining the Mach number for data reduction. The Mach 5 nozzle was calibrated for one total temperature only. Tunnel stagnation pressure and temperature during the Mach 5 tests were therefore used with the inlet spike tip pressure measurements to determine the free-stream Mach number. These Mach-number results correlated well with the Mach number calibrated for one total temperature.

Tests.- The test conditions for the cases used in the present analysis are given in table I. A description of the AIM test plan is contained in reference 7 and the actual test

conditions, test procedures, and facility configurations are discussed in detail in reference 8. During a Mach 6 test the cowl lip was located in two off-design positions (test cases 8 and 9 in table I(a)) to obtain data for an evaluation of effects of this variable on inlet performance. The total pressure was different for some tests for evaluation of effects of altitude simulation on inlet performance. Total temperature was varied to evaluate Reynolds number effect. A Mach 5 test case (number 3 of table I(a)) was conducted with Mach 6 total temperature (approximately 1600 K (2880° R)). This condition simulates Mach 6 flight with a vehicle bow shock ahead of the engine that is equivalent to a two-dimensional shock at an angle of 15°.

Procedures.- After stable tunnel flow was established, the inlet spike was translated to a preselected position. A TV schlieren monitor and inlet pressures were observed to determine that inlet start conditions existed. True steady-state flow conditions without extraneous disturbances within the AIM were obtained by shutting off momentarily all purge gases exhausting from the fuel injectors; purges were reinitiated prior to fuel injection. To achieve the maximum potential of each test, the tunnel flow conditions, inlet spike position, fuel injection schedules, and other relevant parameters were programed for each test and regulated by an automatic tape control system.

HRE-AIM Configuration

AIM.- The AIM is a full-scale, water-cooled, hydrogen-fueled research engine. A pretest photograph of the AIM is shown in figure 2(a), and the AIM is shown partially installed in the HTF in figure 2(b). As evidenced by the photographs, the AIM is axisymmetric with a 45.72-cm-diameter (18-in.) cowl and is 221 cm (87 in.) long. The entire AIM is described in reference 9.

Inlet.- The HRE-AIM inlet is shown schematically in figure 2(c). This inlet was designed to give good internal performance for Mach numbers from 4 to 8 (external drag was not a limiting design constraint). There was a design requirement that the inlet be closed during part of the planned flight test of a flight-weight version of the HRE in order to minimize the cooling requirement. These requirements plus the requirement for increased contraction ratio with increased Mach number resulted in an external-internal compression design with an "upsloping" (5.645° positive slope) throat. This design with a translating spike permitted "shock-on-lip" operation from Mach 6 to 8 with an associated increase in overall geometric contraction ratio $\left((A_C/A_{th})_{overall} = 8.5, 11.7, \text{ and } 13.8 \text{ for } M = 6, 7, \text{ and } 8\right)$, an increase in internal geometric contraction ratio $\left((A_C/A_{th})_{internal} = 2.7, 2.3, \text{ and } 2.1 \text{ for } M = 6, 7, \text{ and } 8\right)$, and an increase in the supersonic combustor area ratio. Also, this design provides the means for inlet starting at low mass flow and low internal contraction. Below Mach 6 (4 to 6) the inlet spike position was to be fixed at the Mach 6 shock-on-lip position. This resulted in increasing flow spillage as the Mach number was reduced from 6 to 4.

The distance between the cowl lip and the spike tip was used as a variable in the present and previous tests. This distance, nondimensionalized by the inlet diameter at the cowl lip, is referred to as the cowl position X_C. Coordinates and radial angles of the AIM inlet are presented in table II and are based on the final contour referred to as the "T" design in reference 2. The cowl coordinates (table II(b)) are for the design shock-on-lip cowl position for Mach 6 $(X_C = 3.872)$. Details of the cowl lip are depicted in the insert of figure 2(c). This sketch shows the location of the most forward point $(X_C, R_C$ coordinate system) on the cowl lip in relation to the 12^o tangent point $(X_{CL}, R_{CL}$ coordinate system generally used in ref. 2). It should be noted that in the present analysis and the analysis of reference 1 the X_C and R_C coordinate system was used.

Relationship between inlet and fuel injectors.- In a subsequent section, "Inlet-Combustor Interaction," the effects on the inlet of fuel injection and burning during the supersonic combustion mode of the AIM are discussed. It is therefore pertinent to describe the location of the supersonic combustion mode fuel injectors in the AIM. Combustor configuration and the fuel injector and ignitor parameters are presented in table III. The inlet-combustor interaction discussed herein pertains to the first-stages (1A and 1B or 1A and 4) and the second-stage (2A and 2C) fuel injectors which are depicted in relation to the inlet in figure 2(c). (Injector 1C was not used in any tests considered in this report.) The staged fuel injection was designed to allow optimum distribution of the fuel in the combustor to obtain a fuel equivalence ratio ϕ of unity during the supersonic combustion mode. During the supersonic combustion mode, it was desired to inject the maximum amount of fuel from the first-stage injectors (1A and 1B) without unstarting the inlet. Injectors 1A and 1B were designed to inject all the fuel at Mach 8.

In the "Inlet-Combustor Interaction" section, results of helium injection during the HRE 2/3-scale inlet tests (ref. 2) and results of an HRE two-dimensional combustor study (ref. 10) are used. Helium was injected in the 2/3-scale inlet tests from the spike at the throat station which was similar to the AIM injector 1A. In table IV, some geometric characteristics of the two-dimensional combustor are presented and compared with those of the AIM combustor at the locations of injectors 1A and 1B. The physical dimensions of the two configurations are about equal; however, the last two items in table IV not being the same for both configurations can be expected to have an effect on the results.

Instrumentation and Data Reduction

Locations of static-pressure orifices for the inlet are listed in table V. Because of instrumentation channel limitations and continual instrumentation malfunctions, some orifices were not used in this analysis as noted in the table.

All data were tape recorded at a data scan rate of 5 frames per second and reduced to engineering units by a data reduction program that incorporated methods described in

reference 7. The performance analysis computer program (ref. 11) computed engine cycle performance, component performance, and various aerodynamic and heat-transfer parameters at selected times.

ANALYSES

Method of Characteristics

A theoretical analysis of the HRE-AIM inlet was performed and reported in reference 1. An updated version of the method-of-characteristics computer program described in reference 12 was used. Results of computer computations for 23 cases were presented in reference 1. For the present analysis, some of these cases corresponded more closely than others to the AIM experimental test conditions. Conditions and results of the most applicable cases are presented in table I(b); the case numbers correspond to those used in reference 1. The Mach 5.15 and 7.25 cases (numbers 9A and 23A) were computed to correspond more closely to the AIM test conditions. The theoretical pressure distributions used herein were obtained from results of the method-of-characteristics computer program. Flow conditions at the inlet throat were processed as described in reference 1 to obtain the mass-weighted average inlet performance parameters used in the present investigation. For some cases the average throat flow conditions were also area weighted and mass-momentum weighted. The results are used in the discussion of inlet performance. An evaluation of the different weighted average procedures is presented in the next section.

Basis for Inlet Performance Comparisons

Since the same performance data are not always available from inlet tests and various theoretical methods, performance parameters such as total-pressure recovery may not always be directly comparable. Such is the situation for the HRE inlet performance data. Different methods were used to derive total-pressure recovery and are reviewed in this section.

Wyatt in reference 13 discussed the errors involved in determining inlet total-pressure recovery by various weighting methods for several theoretical subsonic exit flow profiles for a relatively low free-stream Mach number of about 2. He concluded that the best method to describe inlet performance is to determine an equivalent flow at the measuring station which has the same mass, momentum, and energy and then to derive equivalent flow parameters such as Mach number or static and total pressure. These equivalent flow parameters then would give the best consistent description of the flow at the measuring station and could be used for an efficiency parameter such as total-pressure recovery. The specific equations of Wyatt (ref. 13) are limited to flow profiles of constant static pressure and total temperature, but these restrictions can be eliminated when static-pressure and total-temperature profile data are available. When making

comparisons to see whether one inlet is more efficient than another, the method of data analysis is not as important as consistency. When inlet total-pressure recovery is used as input to a one-dimensional engine cycle program or to a one-dimensional supersonic combustor analysis program (refs. 14 and 11, respectively), an inlet total-pressure recovery is needed which is consistent with the mass, momentum, and energy of the actual flow in order to avoid introducing errors in computations of engine thrust parameters.

The HRE inlet development program has resulted in five variations of inlet total-pressure recovery data (all for the same geometric shape). These are presented for an overall comparison in the present report and are as follows:

(1) Theoretical predictions for the 2/3-scale inlet model (ref. 2)

(2) Experimental results for the 2/3-scale inlet model (ref. 2)

(3) Theoretical predictions for the AIM size inlet (ref. 2)

(4) Additional theoretical predictions for the AIM inlet (present analysis and ref. 1)

(5) The present experimental results from the AIM tests

To make the comparisons shown subsequently in this report, some of the previous data were reanalyzed by means of methods which would allow a direct comparison. For clarity, the four different methods used to derive average total pressure are outlined, and the data to which the methods are applied are noted.

Area-weighted average.- This method requires data on the flow profile at the measuring station. The area-weighted average total pressure is determined by assigning areas upon which the local total pressures in the profile act. The products of the associated assigned areas and total pressures are then integrated and divided by the total area to yield a one-dimensional total-pressure recovery value. This method yields values considered too high when the profiles are highly nonuniform. For parametric comparisons, however, the area-weighted average has been frequently used and was used for one theoretical data point for the AIM inlet at Mach 6.

Mass-weighted average.- Data on the flow profile at the measuring station are also required for this method. The mass-weighted average total pressure is determined by multiplying the local total pressures in the profile by the local mass flow in a given increment, integrating, and dividing by the total mass flow. For many years this method has been used but generally results in values too high, especially when the profile is highly nonuniform. This method and the area-weighted average are considered the least accurate of the methods discussed for deriving total-pressure recovery inputs to one-dimensional computer programs. This method was used to derive the total-pressure recoveries from the theoretical and experimental results for the 2/3-scale inlet (ref. 2), the theoretical results for the AIM size inlet (ref. 2), and the additional theoretical results for the AIM inlet (ref. 1).

Mass-momentum weighted average.- This method also requires computed or experimental data on the flow profile at the measuring station. The method discussed here is essentially that of reference 13 except that the static pressure and total energy are not constant across the inlet throat and are accounted for in the local values of mass and momentum and thereby also in the integral values. The total enthalpy of the air is considered constant outside the boundary layer and equal to the free-stream total enthalpy; the heat transferred to the inlet surfaces results in decreased total enthalpy at the inlet throat in the boundary-layer profile. After the integral values of mass, momentum, and energy are found, the equations are solved for an equivalent one-dimensional flow. The equivalent average total pressure and other flow parameters will describe the inlet efficiency to a one-dimensional computer program within the accuracy of the integrals from the flow profile computations or measurements. This method was applied to an experimental 2/3-scale data point for Mach 6 to use in comparison with the mass-weighted data.

Force-momentum theorem.- This method was used to derive the present theoretical and experimental total-pressure recoveries for the AIM and is somewhat similar to the drag coefficient concept of reference 13 where the inlet drag would be used to evaluate inlet efficiency. The method is based on the momentum theorem, which states that within a given control volume, the change in momentum of a gas stream is equal to the forces acting on the gas. Combining this momentum equation with the continuity and energy conservation equations yields sufficient information to calculate the gas flow properties in the inlet throat. Total pressure is then calculated by means of chemical equilibrium relationships for isentropically stagnated airflow. It is noted that when integrating the static-pressure forces, this method indicates that a data point with higher static pressure on the inside of the cowl (assuming the other parameters remain the same) should result in a higher total-pressure recovery.

This method for assessing inlet (and engine) performance was developed into a computer program that is described in reference 11. The use of the force-momentum method is discussed in the next section, and a brief summary of the inlet analysis portion of the program is included in the appendix.

Procedure for Use of the Force-Momentum Theorem

Measurements necessary for determining inlet experimental performance parameters are surface pressures and temperatures and survey measurements at the throat to obtain total pressures, static pressures, and total temperatures. Survey measurements were not permissible in the AIM test because of the certainty of probe interference with combustor performance. However, the force-momentum method could be used to assess inlet performance using wall static-pressure measurements. After erroneous pressure data were omitted, the performance computer program (ref. 11) averaged the remaining

pressures at each station and longitudinally integrated the wall forces by linear interpolation. Experimental results of the performance computer program are contained in reference 15. Since the pressure instrumentation was limited and some measurements were omitted because of instrumentation malfunction, there is the possibility of differences existing between the experimental performance results and the various weighted average theoretical performance results. Therefore, some theoretical pressure distributions were used as input to the force-momentum performance computer program to obtain theoretical results based on the same analysis method. These results are shown for Mach 5 and 7 in table I(b) and are used in the discussion of the inlet performance; a Mach 6 case was unsuccessful for reasons not fully determined.

RESULTS AND DISCUSSION

Inlet surface-pressure distributions and performance parameters are presented, and they are discussed along with inlet-combustor interaction and inlet unstart conditions. Nominal Mach numbers of 5, 6, and 7 are used in this discussion in place of the actual values of 5.15, 6.05, and 7.25.

The schematic of figure 2(c) shows the spike tip bow shock and the cowl leading-edge shock reflecting through the internal channel. Pressure distributions are discussed in two parts: (1) the undisturbed flow along the spike upstream of the impingement of the cowl leading-edge shock upon the spike (region "A" shown in fig. 2(c)), and (2) the internal flow downstream of the cowl leading edge (region "B"). The internal-flow pressure distributions are employed in discussions of combustor interaction upon the inlet. Pressure distributions for the entire inlet were used in the inlet force-momentum performance computations, and the results are discussed in terms of total-pressure recovery, throat Mach number, and kinetic energy efficiency.

Inlet Undisturbed Surface Pressures

A comparison of experimental and theoretical pressure distributions along the spike surface is shown for Mach 6 in figure 3. The distribution shown extends to the point of impingement of the cowl lip bow shock upon the spike (undisturbed region) as shown in the shock schematic of figure 3(a). Experimental pressure data from the AIM tests are shown in figure 3(b) as the open symbols and exhibit good agreement with theory. Since the AIM had pressure orifices on the spike upstream of the cowl leading edge only at $X = 1.6$ and 3.4, which is a rather large increment, experimental results in this region for the 2/3-scale inlet model tests reported in reference 2 are included. These 2/3-scale results are shown as the solid symbols in figure 3(b) and also show good agreement with the present theoretical curve. Excellent agreement was also attained for the AIM at Mach 5 and 7.

Internal-Flow Pressures

Static pressures on the inner surface of the cowl and on the spike surface downstream of the cowl leading edge are presented in figures 4 to 7. In these figures the pressure distributions on the cowl inner surface are shown in the top portion and the spike pressure distributions are shown in the bottom portion. Shown in the center portion of figures 4, 5, and 7 are the theoretical internal "shock trains" correlated to the X-scale of the pressure distributions; also depicted are the inlet throat station and the first-stage fuel injectors. The theoretical distributions obtained from the computer program of reference 12 exhibit discontinuities which correspond to the shock impingements on the cowl and spike surfaces. Pressure discontinuities in the theoretical distributions connected by the short-dashed lines correspond to the effect of coalesced characteristic rays continuing downstream through the internal passage. These coalesced ray discontinuities however do not have associated entropy gains or total-pressure losses as discussed in reference 1.

The theoretical results generally predict the experimental pressure levels. However, pressure trends or discontinuities exhibited by the theoretical trends are not always experimentally evident. The lack of explicit experimental discontinuities is thought to be the result of local boundary-layer separation at shock impingement points and/or data scatter. Various symbols represent the experimental pressures in the different radial planes and also show evidence of data scatter.

Inlet performances were based on average measured surface pressures (after erroneous pressure data were deleted) used in the one-dimensional force-momentum computer program. The solid-line pressure distributions shown in figure 4 are representative of the distributions used in the computer program of reference 11 (distributions used in each analyzed data point are tabulated in ref. 15). Such experimental data fairings can result in values of inlet performance parameters different from values obtained from theoretical pressure distributions; these differences are discussed in the section, "Inlet Performance."

During Mach 6 and 7 tests the Reynolds number was varied by changing the free-stream total pressure and total temperature, respectively. Results indicated that Reynolds number had a negligible effect on inlet steady-state static pressures and therefore is not discussed further. Effects of free-stream Mach number, cowl position, angle of attack, and vehicle-inlet integration on inlet static-pressure distributions are discussed in the following sections. Also discussed is the effect of the interaction of the inlet and combustor upon one another.

Effect of Mach number.- The effect of the free-stream Mach number on the internal surface-pressure distributions can be assessed by comparison of distributions at Mach numbers of 5, 6, and 7 shown in figure 4. The cowl positions for both Mach 5 and 6 are the same $\left(X_C \approx 3.9\right)$ as planned and result in relatively large flow spillage $\left(\dot{m}/\dot{m}_\infty = 0.867\right)$

at Mach 5 and nearly full capture $\dot{m}/\dot{m}_\infty = 0.986$ of the available mass flow at Mach 6. The cowl position was different $(X_C \approx 4.1)$ for Mach 7 to allow nearly full capture $(\dot{m}/\dot{m}_\infty = 0.991)$ of the available mass flow.

From comparison of the pressure distributions in figure 4, it is evident that Mach number has negligible effect on relative pressure rise in that the inlet compression causes about the same relative pressure rise for all three free-stream Mach numbers. That is, the internal compression increases the undisturbed pressure ratio ahead of the cowl lip (X = 4.0) by a factor of about 5 by the time the throat is reached; for example, at Mach 6 (fig. 4(b)) the undisturbed pressure ratio at $X = 4.0$ is about 0.005 and at $X = 4.4$ the value is about 0.025 or a ratio of 5.

Comparison of the distributions for the three Mach numbers shows that the experimental pressures were most accurately predicted for Mach 6, especially along the cowl inner surface. Experimental pressures on the cowl at X greater than 4.4 do not appear to be well predicted, the result of a displacement of shock impingements on the cowl from the theoretical impingement points. At Mach 7 the experimental trend for the cowl appears different from theory, possibly because the experimental shock train has immediate shock reflections unlike the theoretical delayed reflections. (See shock sketch in fig. 4(c).) With the cowl position $(X_C \approx 4.1)$ for Mach 7, the geometric internal passage height is less than the height for Mach 6, and shock impingements and reflections would be expected to be more closely spaced at Mach 7; thus, because of the limited number of pressure orifices and data scatter, explicit peaks and valleys in the experimental data are not evident.

Effect of cowl position.- During the Mach 6 tests the cowl position was varied from the near shock-on-lip position, $X_C = 3.911$, to mass-flow-spillage positions, $X_C = 4.075$ and 4.163, to evaluate the effect of this variable on inlet performance and in turn on engine performance. Movement of the inlet spike forward with respect to the cowl (increased X_C) increased the geometric contraction ratio and decreased the internal duct height. Although the mass flow captured decreased, the aerodynamic contraction ratio $(A_C/A_{th})(\dot{m}/\dot{m}_\infty)$ increased to a maximum value of 10.1 at Mach 6 followed by a decrease in this ratio. (See insert plot in fig. 5.)

Figure 5 presents the static-pressure distributions for three cowl positions: $X_C = 3.911$ which is the position for capture of maximum mass flow, $X_C = 4.075$ which is the position for maximum aerodynamic contraction ratio, and $X_C = 4.163$ which is for minimum mass-flow capture. Cowl positions $X_C = 3.911$ and 4.163 result in about the same aerodynamic contraction ratio.

Internal duct height decreases with increased X_C, and thus the stationwise spacing of the shock reflections is reduced. As a result, peaks and valleys of the experimental pressure distributions are difficult to discern as previously discussed. The overall

pressure levels for lower mass flow (figs. 5(b) and 5(c)) are slightly higher than the full capture case, especially on the forward portion of the cowl inner surface.

Angle-of-attack effect.- Static-pressure distributions for Mach numbers of 5, 6, and 7 with the model at an angle of attack of 3° are shown by the closed symbols in figure 6. Spike pressures in the undisturbed region ($X \approx 3.8$ to 4.2) are slightly increased on the windward side ($\theta = 0^{\circ}$) and decreased on the leeward side as would be expected. The differences in the internal surface pressures on the windward and leeward sides of the model downstream of the cowl shock are larger than those on the spike external surface.

Effect of vehicle-inlet integration.- Original, unfulfilled HRE plans were to flight test an engine on the X-15-2 airplane. During such flight tests the engine would have been in the vehicle flow field at an angle of attack from 0° to 10°.

During the AIM tests the maximum achievable total temperature was about 1700 K (3060° R), sufficient for simulating Mach 6 flight. Therefore, to simulate vehicle flow-field conditions downstream of a vehicle bow shock, test conditions were set for $M_{\infty} \approx 5.15$ at $T_{t,\infty} = 1667$ K (3000° R) and $p_{t,\infty} = 20.4$ atm. The total pressure was lower than desired because of heat-transfer limits of the facility nozzle. These conditions approximately simulate the conditions behind the bow shock of a vehicle having a 10° half-angle conical nose flying at an angle of attack of 0°, Mach 6, and an altitude of 30.2 km (99 000 ft) rather than full simulation at 23.5 km (77 000 ft).

Surface static-pressure distributions and theoretical internal shock patterns for these simulated vehicle flow-field conditions compared with those for the inlet without any shock ahead of the inlet are shown in figure 7. The internal theoretical shock patterns show evidence of slight differences which in turn yield differences in the pressure distributions. Pressure ratios on the spike for the simulated flow-field condition are predicted to be lower than for the free-stream condition; however, experimental pressure ratios on the spike are about equal for both conditions.

Inlet-Combustor Interaction

An objective of the AIM tests was to determine the interactions of the engine components on one another when integrated together as a full-scale unit. The interactions of the inlet on the combustor and the combustor on the inlet are both discussed.

Inlet interaction on combustor.- The interaction of the inlet on the combustor is the continuation of the inlet shock-wave system into and through the combustor as indicated by the theoretical internal shock diagrams in previous figures and figure 8 and results in associated total-pressure losses in the combustor. This type of flow is inherent in supersonic and hypersonic inlets. Such flow delivered to the combustor is difficult to

simulate in direct-connect combustor component tests; thus it is difficult to predict engine combustor efficiency from combustor component tests.

Combustor interaction on inlet.- During normal engine operation the combustor did not interact on the inlet. Inlet operation was affected by the combustor however when large amounts of fuel were injected from the engine first-stage fuel injectors. Ignitors were necessary to achieve combustion with first-stage fuel injection only. As fuel is injected and combustion occurs, pressures in the inlet increase at the throat station and slightly upstream (about one throat height) of the throat as indicated in figure 8 for Mach 6.

Effects of injection and combustion on the inlet pressures are more easily recognized in figure 9 where the ratios of pressures with combustion to pressures without combustion are shown. The cowl throat pressure increased by a factor of 3 because of fuel injection from the first stage; this increase occurred with the maximum first-stage injection just prior to inlet unstart. There was not a static-pressure orifice at the spike throat station, but straight-line interpolations indicate an increase on the order of 0.5 as a result of fuel injection and combustion. The greatest pressure increases on the spike in figure 9 are downstream of the throat and the 1A fuel injector. Pressure rises recorded for the cowl in figure 9 appear opposite fuel injector 1A on the spike, and conversely, the spike pressure rises are opposite fuel injector 1B on the cowl. This trend suggests that the fuel jets penetrated across the duct to the opposite wall. However, there were no hot-spot flow patterns to suggest such an impingement on the cowl surface of injector 1A jets. These pressure changes and the associated internal shock train changes are the result of (1) mass addition of the fuel jets that restricts the internal flow path, possibly causes local boundary-layer separation, and creates flow compression, and (2) heat addition from fuel combustion that decelerates the flow and creates additional flow compression. Pressure rises at and upstream of the throat are insignificant and are not shown for ϕ less than 0.3. Any boundary-layer-separation phenomenon is thought to be three-dimensional in character around the individual injector holes at low fuel flows ($\phi < 0.3$) and to approach a two-dimensional or wedge-type separation at high fuel flows. It is believed that the pressure increases become significant when such a wedge-type separation occurs.

In figure 10 the effect of the AIM inlet-combustor interaction on the cowl surface throat pressure is shown for Mach 6 and 7. The pressure at this station was chosen (based on figs. 8 and 9) as an index of the pressure rise associated with inlet unstart. Pressure-rise trends associated with fuel injected from the AIM first-stage fuel injectors with ignitors are shown for Mach 6 in figure 10(a). Shown for comparison with the AIM trends is the pressure rise at the combustor entrance (inlet throat) as a result of increase in fuel flow in two-dimensional direct-connect combustor tests that simulated

conditions for Mach 6 flight (reported in ref. 10). During Mach 6 component tests of the 2/3-scale HRE inlet model (ref. 2), helium was injected from the spike near the inlet throat. The helium injector flow was increased until the inlet unstarted at a throat pressure rise of about 2.5; this pressure-rise limit is shown in figures 10(a) and 10(b). The rates of pressure rise in the two-dimensional combustor and the AIM combustor are about the same; however, the AIM pressure rise is delayed. The physical differences between the two-dimensional and AIM combustors were discussed in the apparatus section and are tabulated in table IV. The physical dimensions are about equal, but the interdigitized arrangement of the two-dimensional combustor injectors would result in more flow blockage than the AIM inline arrangement and possibly in the differences in the pressure-rise trends. Another factor may have been side-wall effects in the two-dimensional combustor. If the 2/3-scale inlet pressure-rise limit of 2.5 is assumed for the two-dimensional combustor, inlet unstart would occur at a fuel equivalence ratio of 0.273. The AIM pressure increase did not begin until $\phi \approx 0.3$, and inlet unstart occurred at $\phi \approx 0.35$ after the pressure had increased about 2.9 times the undisturbed pressure. The AIM inlet unstart at $\phi \approx 0.35$ closely approaches a predicted value obtained from one-dimensional ramjet cycle calculations (ref. 16). These calculations were performed to determine the fuel equivalence ratio which, by the combination of mass addition and combustion heat release, would choke the combustor with the selected combustor area distribution for Mach 6 operation. These calculations indicated that a first-stage value of ϕ of 0.38 (shown in fig. 10(a) as vertical dashed line) would choke the combustor and, thereby, unstart the inlet.

Effects on the throat cowl pressure of fuel injection from two stages of injectors are shown for Mach 6 in figure 10(b). Prior data on the 2/3-scale inlet pressure-rise limit, mentioned above, and on two-stage injection during two-dimensional combustor tests indicated that the first-stage value of ϕ should be limited to 0.18 with the remaining fuel injected from the second-stage injectors in order to be certain to avoid inlet unstart. For the case shown in figure 10(b), fuel injection was increased rapidly to a total ϕ of about 1.0 where 0.18 was injected from the first-stage injectors (1A and 1B) and the remainder of the fuel was injected from the second-stage injectors. It was observed that autoignition of the first-stage fuel occurred as a result of the second-stage fuel injection. Fuel flow was then increased from the first-stage fuel injectors and decreased from the second-stage injectors, ϕ_{tot} being maintained at approximately 1.0. With this procedure the inlet unstarted when the first-stage value of ϕ was about 0.34, and the pressure on the cowl surface increased about 2.6 times the undisturbed pressure. These values of first-stage fuel equivalence ratio and pressure rise at inlet unstart are very nearly equal to those for fuel being injected from the first-stage injectors only. This indicates that fuel staging has little effect on inlet unstarting and that injection nearest the throat is the dominant factor. Fuel staging does, however, result in increased inlet throat pressures at lower

first-stage values of ϕ. The pressure-rise values shown in figures 10(a) and 10(b) are about the same as those associated with a purely aerodynamic boundary-layer separation caused by a short-radius turn at a Mach number similar to the inlet throat Mach number. It is concluded that the unstart mechanism is controlled by a boundary-layer separation phenomenon which is also slightly affected by second-stage fuel injection, perhaps through a continuation of the separated area from the first-stage location to the second-stage location.

From results similar to those shown in figure 10(b), the fuel equivalence ratio for the first-stage injector during staged-injection engine performance tests was selected to be 0.24. This value would allow ignition from stage interaction and assure stable inlet operation.

Effects of first-stage fuel injection upon the cowl throat pressure at a free-stream Mach number of 7 are shown in figure 10(c). Downstream ignitors were employed but it appeared that ignition did not occur until the injector flow rate was sufficient to generate enough aerodynamic pressure and temperature rise to ignite the fuel (ignition indicated in fig. 10(c) by arrows). The ignition was somewhat more delayed when the AIM was positioned at an angle of attack of 3°. The inlet unstarted for $\alpha = 3^{\circ}$ at $\phi = 0.482$, but for $\alpha = 0^{\circ}$, the inlet did not unstart with the amount of fuel injected (maximum $\phi_1 = 0.57$ which was lower than planned). At $\alpha = 0^{\circ}$, the inlet unstart limit was therefore not determined.

Figure 10(d) presents the pressure rise at the cowl throat as fuel is injected from two stages at Mach 7. The procedure was similar to the Mach 6 two-stage injection test (fig. 10(b)) in that a nearly constant total value of ϕ of 0.95 was maintained as the first-stage (injectors 1A and 4) value of ϕ was increased from 0.18 to 0.52 (lower than planned). Cowl throat pressure increased about 1.57 times for the maximum first-stage fuel injection ($\phi_1 = 0.52$). An inlet unstart did not occur with this amount of throat pressure increase and an inlet unstart limit was not determined. The rate of increase is much less than for Mach 6 (fig. 10(b)). A major factor that could cause the lower rate of pressure increase is the greater longitudinal separation between the spike and cowl first-stage injectors; at Mach 6 this nondimensionalized separation distance is 0.08 and at Mach 7 the distance is 0.84.

Inlet unstart.- Interactions of the combustor on the inlet, as just discussed in the previous section, did not affect inlet operation up to the point of inlet unstart; that is, inlet operation was stable and inlet unstarts were instantaneous. The inlet in a started, stable operating condition is typically represented in the schlieren photograph of figure 11(a), and the associated experimental pressure distributions for the spike and cowl are also shown. Inlet pressures at and slightly upstream of the throat could be affected by first-stage fuel injection and combustion without unstarting the inlet. However, when

the effect became sufficient to cause boundary-layer separation, the inlet would become unstarted. (See schlieren photograph in fig. 11(b).) Inlet unstarts create large pressure increases in the inlet internal flow as shown by the pressure distribution in figure 11(b), and for Mach 6, spike pressures, detected by the static-pressure orifice at $X = 1.6$, are disturbed as far forward as midway between the spike tip and the cowl lip. At Mach 7 the spike pressure disturbances did not propagate as far forward; the most forward point of detection was at the $X = 3.4$ measuring station. Since the shock-on-lip cowl position for Mach 6 ($X_C \approx 3.91$) is further forward relative to the spike tip than for Mach 7 ($X_C \approx 4.06$), the height from the cowl lip to the spike surface is greater and the internal contraction is also greater. Therefore, for a Mach 6 unstart the flow disturbance must extend further forward on the inlet spike to achieve a spillage flow condition which will accommodate the greater blockage downstream (similar to separation caused by a forward-facing step).

For normal Mach 6 and 7 shock-on-lip operation, the inlet geometric internal contraction ratios (2.7 and 2.3, respectively) exceed the value (1.4 to 1.5) that would allow an inlet start (based on the Kantrowitz method discussed in refs. 2, 17, and 18). To restart the inlet after an inlet unstart at Mach 6 required shutoff of the fuel flow and translation of the spike forward toward closeoff to approach an internal contraction ratio of 1.4. However, for Mach 7, the inlet restarted without spike movement when the fuel was shut off even though the geometric internal contraction ratio exceeded the Kantrowitz criterion by 50 percent. A similar restart at a value higher than the Kantrowitz criterion was obtained at Mach 8 during the 2/3-scale inlet model test as reported in reference 2. The starting mechanism is considered to be a function of the internal contraction ratio and the ratio of boundary-layer height to duct height at the cowl lip as discussed in reference 17.

During AIM combustor analysis (ref. 9) it was noted that the pressure rise associated with the initial fuel injection at the inlet throat occurred within a length of 2 or 3 duct heights, while the maximum pressure rise of about 10 associated with the two-stage supersonic combustion process occurred over a length of about 10 duct heights. The spread of the pressure rise is probably the result of a separated flow region in addition to the heat release rate and staged fuel injection. It is important to note that with these types of pressure gradients in the AIM, stable operation was achieved without a step in the duct at the point of fuel injection. The smooth wall appears to have been a suitable design choice for the AIM, although others (ref. 19) advocate the use of a rearward-facing step at the inlet-combustor interface to help isolate the inlet.

Inlet Performance

Inlet performance parameters considered herein for the HRE supersonic combustion mode are inlet total-pressure recovery, throat Mach number, and kinetic energy efficiency.

A correlation of total-pressure recovery with throat Mach number is also discussed. The experimental analysis depends on experimental surface pressures such as those shown in figures 3 to 7. These pressures were averaged at the axial stations (representative distributions shown by the experimental fairing in fig. 4) by the performance computer program (ref. 11) which then integrated the wall forces by linear interpolation as discussed in the analyses section and the appendix. Theoretical inlet flow conditions were obtained by the method-of-characteristics computer program (ref. 12). Throat station profiles of these theoretical flow conditions were used to obtain inlet performance. Various levels of performance were obtained by different methods of weighted averaging as discussed in the analyses section.

Effects of wall cooling on the AIM inlet efficiency are thought to be similar in magnitude to those encountered for the HRE 2/3-scale inlet model (ref. 2); that is, approximately 2 to 4 percent of the total energy of the captured flow was removed by wall cooling. Total enthalpy ratios for the AIM theoretical computations shown in table I(b) exhibit about the same percentage removed. Specific AIM experiments were not conducted to investigate the effect of varying the coolant flow ratio; thus, the actual influence of wall cooling on the performance results could not be derived from the data.

Inlet performance results for the subsonic mode of combustion are not discussed in this report. The AIM performance computer program (ref. 11), however, yields such inlet performances which are discussed briefly in reference 9. All results of the AIM performance program are contained in reference 15.

Kinetic energy efficiency.- Experimental results for HRE-AIM kinetic energy efficiency η_{KE} shown in table I(a) do not indicate any particular trend with respect to free-stream Mach number or various cowl positions; therefore, no curves are presented. Theoretical η_{KE} results of reference 1 similarly did not exhibit any particular trend. The theoretical values were averaged in reference 1 to yield a value of 0.931, and the average of the six mass-weighted theoretical cases in table I(b) is 0.937. The average of the two force-momentum-derived values of table I(b) is 0.928. The average value of the experimental results at an angle of attack of 0° in table I(a) is also 0.937.

Total-pressure recovery.- Theoretical and experimental inlet total-pressure recovery as a function of free-stream Mach number is presented in figure 12(a). Results of various weighted averaging methods for obtaining theoretical pressure recovery are shown at Mach 6. These results show the different levels of values as discussed in the analyses section. The mass-weighted theory (method also used in ref. 1) exhibits a decreasing trend with an increase in Mach number. There were only two theoretical points (table I(b)) available from the force-momentum method which has a similar decreasing trend with an increase in Mach number. A fairing through these two points was therefore fashioned after the mass-weighted curve. The present experimental values show the same decreas-

ing trend. It is noted that the experimental and theoretical data for Mach 7 are for off-design total temperature. (See table I.) Lower force-momentum-derived values, both theoretical and experimental, with respect to the mass-weighted values may possibly be the result of limited pressure measurements (theoretical points were input at the same X-locations as the AIM pressure orifice locations) as discussed in the analyses section. The AIM experimental values were about 10 percent lower than the force-momentum-derived theoretical results at Mach 5 and 6 and about 28 percent higher at Mach 7. Since the force-momentum method depends upon the surface-pressure distributions, it can be seen by comparing the experimental and theoretical pressure distributions in figure 4 how these differences can occur. On the cowl the theoretical and experimental distributions are very similar for all three Mach numbers. However, the spike distributions are very dissimilar because of the inability to predict correctly the boundary-layer shock interaction and, thereby, the shock-wave reflections. These dissimilarities would influence the performance results because the location of the pressure rise becomes important when the pressure area integration is performed. The theoretical static-pressure distributions for Mach 5 and 6 resulted in less momentum loss (greater derived total-pressure recovery) than experiment and a greater momentum loss for the theoretical distribution at Mach 7. This observation agrees with the overprediction of pressure recovery at Mach 5 and 6 and the underprediction at Mach 7.

AIM experimental results at an angle of attack of 3° are also shown in figure 12(a) where they exhibit degradation of the inlet total-pressure recovery as a result of angle-of-attack operation. Pressure recovery (table I(a)) is reduced on the order of 13, 32, and 33 percent for Mach 5, 6, and 7, respectively, because of increasing the angle of attack to 3°.

An analysis of the effect of Reynolds numbers on the total-pressure recovery was conducted, and no effect was found within the limited range of the data. There was a small decrease, about 8.5 percent, in the recovery at Mach 5 when the total temperature was increased from Mach 5 simulation to Mach 6 simulation (1222 K to 1636 K (2200° R to 2945° R)).

In reference 1, theoretical results yielded a pressure recovery trend as a function of cowl position shown by the upper curve in figure 12(b). AIM tests at various cowl positions were performed only for Mach 6, and comparison of the experimental data with the theoretical trend of reference 1 shows that the experimental results were lower than predicted. The reference 1 trend was mass weighted. Since a trend was not available from theoretical force-momentum calculations, a curve was obtained as follows: the theoretical force-momentum method yielded a Mach 6 interpolated pressure recovery of 0.41 (fig. 12(a)); this value is about a 30-percent reduction from the theoretical mass-weighted value at Mach 6; therefore, the theoretical mass-weighted value at the shock-on-lip cowl

position in figure 12(b) was reduced by 30 percent, and then a trend as a function of cowl position was faired through this reduced value parallel to the mass-weighted trend. The resultant curve agrees reasonably well with the experimental results. The total-pressure recovery increased until a cowl position $(X_C \approx 4.07)$ was reached where the maximum inlet aerodynamic contraction ratio occurred. Then both theoretical and experimental values of total-pressure recovery decreased with increased X_C.

Inlet throat Mach number.- HRE-AIM experimental and theoretical throat Mach numbers are presented in figure 13. The theoretical mass-weighted average results were presented in reference 1 and are shown as the upper curve in figure 13(a). A similar theoretical force-momentum trend was desired for comparison with the AIM experimental results. Such a trend was obtained (lower curve in fig. 13(a)) by averaging the differences between the mass-weighted and the force-momentum-derived throat Mach numbers at Mach 5 and 7 and then using this average reduction (16 percent) to yield the force-momentum trend. The theoretical trends, as well as the experimental results, show an increase in throat Mach number with an increase in free-stream Mach number. Experimental values are in good agreement with the force-momentum-derived trend; predictions are 0.5 percent high at Mach 5, less than 0.5 percent high at Mach 6, and 2.5 percent low at Mach 7. Simulation of the engine located downstream of the vehicle bow shock at Mach 5 (flagged symbol) slightly increased throat Mach number. The degradation of throat Mach number with the inlet positioned at an angle of attack of 3° is also shown in figure 13(a) by the double-flagged symbols; reductions of 5.5, 12.5, and 10.0 percent are evident for Mach 5, 6, and 7, respectively.

Theoretical mass-weighted average trends at different free-stream Mach numbers were presented in reference 1 for the variation of throat Mach number with cowl position; the trend for Mach 6 is presented in figure 13(b). The value at the shock-on-lip cowl position $(X_C = 3.91)$ was reduced 16 percent as discussed for figure 13(a), and a trend parallel to the reference 1 trend was assumed to represent the theoretical force-momentum values. The theoretical trends show a decrease in throat Mach number with increased X_C, a negative 2.4 slope. Experimental results do not agree with this trend in that the levels of the three data points change very little with cowl position.

Correlation of throat total-pressure recovery with throat and free-stream Mach numbers.- The AIM experimental results showed reasonably good agreement with force-momentum-derived theoretical results; the poorest agreement occurred for the off-design cowl positions. Reference 9 presents a good correlation of total-pressure recovery with free-stream and throat Mach numbers. The correlation is shown in figure 14 and indicates that the more the flow is compressed (lower throat Mach numbers) the greater the total-pressure loss, but this observation is expected for any reasonably efficient inlet. All the data of table I(a) are used in the correlation including those for various cowl

positions, different Reynolds numbers, and angles of attack of 0° and 3°. There are two points that did not correlate well, one at Mach 6 for the midcowl position and the other at Mach 5 representing the engine located downstream of a vehicle bow shock (experimental Mach 6 flight temperature).

It is interesting to note that if the curves for free-stream Mach numbers of 5 and 6 are extrapolated, data for an entirely different inlet concept (ref. 20) correlate with these HRE results. That is, at Mach 5 and 6 for the three-dimensional inlet of reference 20 the values of total-pressure recovery are 0.675 and 0.600, respectively, and the values of throat Mach number are 2.4 and 3.0, respectively.

CONCLUDING REMARKS

Tests of a full-scale Hypersonic Research Engine (HRE) Aerothermodynamic Integration Model (AIM) have been successfully completed in the Lewis Hypersonic tunnel facility at the Plum Brook Station. Inlet surface pressures were measured and have been used in conjunction with correlations of other parameters to obtain estimates of the HRE-AIM inlet performance.

During the present analysis, static pressures measured on the AIM inlet surfaces showed reasonable agreement with theoretical predictions except in regions where the theory predicts large pressure discontinuities. Limitations in the theoretical boundary-layer interaction model, especially where separations may occur, are thought to explain this discrepancy. Variations of Reynolds number had no apparent effect on the static-pressure distributions or on inlet performance within the limited range of the data. Total-pressure recovery decreased about 8.5 percent at Mach 5 when the total temperature was increased from about 1200 K to 1600 K (2160° R to 2880° R) to simulate an engine located downstream of a vehicle bow shock at a free-stream Mach number of 6. Engine angle of attack had a greater effect on the inlet internal surface pressures than on the spike external surface pressures. An angle of attack of 3° decreased the experimental total-pressure recovery for Mach numbers of 5, 6, and 7 on the order of 13, 32, and 33 percent, respectively.

Experimental data were analyzed with a one-dimensional force-momentum theorem. Theoretical predictions of inlet throat total-pressure recovery based on the same theorem were about 10 percent higher than the AIM experimental values at Mach 5 and 6 and 28 percent lower at Mach 7. Throat Mach numbers as a function of free-stream Mach number were predicted within 2.5 percent of the experimental data. Throat total-pressure recovery as a function of cowl position generally followed the same trend as theory; however, experimental throat Mach numbers did not exhibit the decreasing trend indicated by theory as the inlet cowl position was moved farther from the inlet spike tip.

Previous predictions of inlet unstart because of pressure disturbances that resulted from fuel injection and combustion are pessimistic. Results of the present analysis indicated that an inlet unstart condition can be caused only by excessive fuel injection and combustion near the inlet throat. This analysis also indicated that fuel staging (distribution of the fuel injection through the combustor) had little effect on inlet unstarting. It is evident from the analysis that injection nearest the throat is the dominant factor and that the inlet unstart mechanism is controlled by a boundary-layer separation phenomenon. During inlet unstart, pressure disturbances moved farther forward on the inlet spike at Mach 6 than at Mach 7, probably because of a greater height from the cowl lip to the spike surface and greater geometric internal contraction at Mach 6. When the inlet unstarted at Mach 7, it could be restarted by simply reducing the fuel flow without any translation of the spike; at Mach 6 the spike had to be translated to obtain a lower internal geometric contraction ratio to restart the inlet. The analysis showed that an inlet restart was achieved even though the geometric internal contraction ratio was about 50 percent higher than the value indicated by the Kantrowitz criterion that would allow an inlet start.

In conclusion, it should be noted that the inlet operation was stable during the AIM tests over a wide range of fuel-to-air equivalence ratio. This stable operation was achieved without a step in the wall at the combustor entrance (inlet throat) even though a step is advocated by other researchers.

Langley Research Center
National Aeronautics and Space Administration
Hampton, Va. 23665
March 26, 1976

APPENDIX

INLET PERFORMANCE ANALYSIS

Inlet performance parameters were obtained from the performance analysis computer program described in reference 11 using methods described in reference 7. The program uses a one-dimensional force-momentum balance equation combined with equations related to laws of conservation and thermodynamic properties for equilibrium air.

The momentum equation used to determine conditions at the inlet throat, which is the combustor entrance, with the areas being projected normal to the free stream is expressed as follows:

$$F_{th} = \dot{m}V_{th} + p_{th}A_{th} = \dot{m}V_{\infty} + p_{\infty}A_C\left(\frac{\dot{m}}{\dot{m}_{\infty}}\right) + \int_{Cowl} p\,dA - \int_{Spike} p\,dA$$

$$+ \int_{\substack{Spillage \\ streamline}} p\,dA - \int_{Cowl} C_f q_l \cos\xi\,dA - \int_{Spike} C_f q_l \cos\xi\,dA$$

$$- C_{D,tip}q_{\infty}A_{tip} - C_{D,lip}q_l A_{lip} \qquad (A1)$$

where $\dot{m}/\dot{m}_{\infty}$ is a function of M_{∞}, X_C, and α, and

$$\dot{m} = \rho_{\infty}V_{\infty}A_C\left(\frac{\dot{m}}{\dot{m}_{\infty}}\right)$$

Note that $\int p\,dA$ for the cowl is positive in the assumed coordinate system because the drooped cowl yields frontal area opposite that of the spike.

All parameters involved in equation (A1), with the exception of spillage drag, skin friction coefficient, and drag coefficients for the spike tip and cowl lip, were intended to be products of direct measurements or derivations thereof. Airflow calibration tests were to be conducted with a flow metering duct installed but were canceled; thus, the determination of inlet mass-flow ratios $\dot{m}/\dot{m}_{\infty}$ relied upon the theoretical results of reference 1. The validity of this approach was substantiated by the fact that satisfactory correlations were obtained between theory and experiment with the 2/3-scale inlet model. Inlet airflow was calculated from the theoretical mass-flow ratio (a function of spike position, wind-tunnel Mach number, and angle of attack) and the value of mass flow per unit area in the wind tunnel.

APPENDIX

Integrated wall forces in the momentum equation were based on linear interpolation in the axial direction of measured static pressures. When more than one pressure reading was available at a given station, an arithmetic average was used.

The spillage streamline pressure area integral was calculated from

$$\int_{\substack{\text{Spillage}\\ \text{streamline}}} p\,dA = q_\infty A_C C_{D,A} + p_\infty A_C\left(1 - \frac{\dot{m}}{\dot{m}_\infty}\right)$$

using theoretical values (ref. 1) of $\dot{m}/\dot{m}_\infty$ and the additive drag coefficient $C_{D,A}$, a function of $\dot{m}/\dot{m}_\infty$. (Note that A_C is the cross-sectional area at the cowl lip.) Angle-of-attack corrections, based on HRE 2/3-scale inlet test results, were affected by a mass-flow ratio correlation given in reference 2.

Drag coefficients for the blunted portions of the inlet spike tip and cowl lip were obtained by numerical pressure integration on the tip and lip. Pressure distributions on the blunted portions were taken from typical Mach 6 cases computed by the computer program of reference 12.

The friction coefficient is calculated by the method of reference 21 for a turbulent boundary layer by using

(1) Flat-plate analysis for the cowl internal surfaces

(2) Flat-plate analysis corrected for conical surface for the inlet spike (the correction reduced the flat-plate Reynolds number by 1/2)

Once the inlet throat thrust function is determined, an effective Mach number and related effective static pressure across the throat area, which simultaneously satisfy the total energy, mass flow, and momentum at that station, are derived. An effective total pressure is then obtained by isentropic calculation for equilibrium air at stagnation conditions.

The flow characteristics derived in this way are those that may be obtained if the actual nonuniform flow could be mixed and converted into a uniform flow in a constant area duct without wall friction losses. Thus, mixing losses are inherently contained in these average values. This fact must be kept in mind when comparing these results with other tests or theoretical analyses in which other methods of weighted averaging have been used.

REFERENCES

1. Andrews, Earl H., Jr.; Russell, James W.; Mackley, Ernest A.; and Simmonds, Ann L.: An Inlet Analysis for the NASA Hypersonic Research Engine Aerothermodynamic Integration Model. NASA TM X-3038, 1974.

2. Pearson, L. W.: Hypersonic Research Engine Project – Phase IIA. Inlet Program. Final Technical Data Report. AP-69-4883 (Contract NAS 1-6666), AiResearch Manufacturing Co., Mar. 27, 1969. (Available as NASA CR-66797.)

3. Hube, Frederick K.: Tests of a One-Third-Scale NASA Hypersonic Research Engine Inlet at Mach Numbers 6 and 8. AEDC-TR-68-28, U.S. Air Force, Mar. 1968. (Available from DDC as AD 388 036.)

4. Hube, Frederick K.; and Bontrager, Paul J.: Wind Tunnel Tests of a Two-Thirds Scale NASA HRE Inlet at Mach Numbers 4, 5, 6, and 8. AEDC-TR-69-9, U.S. Air Force, Feb. 1969. (Available from DDC as AD 395 666.)

5. Molloy, John K.; Mackley, Ernest A.; and Keyes, J. Wayne: Effect of Diffusers, Shrouds, and Mass Injection on the Starting and Operating Characteristics of a Mach 5 Free-Jet Tunnel. NASA TN D-6377, 1971.

6. Cullom, Richard R.; and Lezberg, Erwin A.: Calibration of Lewis Hypersonic Tunnel Facility at Mach 5, 6, and 7. NASA TN D-7100, 1972.

7. Engineering Staff: Hypersonic Research Engine Project – Phase II. Aerothermodynamic Integration Model Test Plan. NASA CR-132497, 1972.

8. Andersen, W. L.; and Kado, L.: Hypersonic Research Engine Project – Phase II. Aerothermodynamic Integration Model (AIM). Test Report. NASA CR-132655, 1975.

9. Engineering Staff: Hypersonic Research Engine Project – Phase II. Aerothermodynamic Integration Model Development. Final Technical Data Report. NASA CR-132654, 1975.

10. Engineering Staff: Hypersonic Research Engine Project – Phase II. Combustor Program. Final Technical Data Report. Doc. No. AP-70-6054 (Contract No. NAS 1-6666), AiResearch Manufacturing Co., Mar. 23, 1970. (Available as NASA CR-66932.)

11. Gaede, A.: Hypersonic Research Engine Project – Phase II. Aerothermodynamic Integration Model (AIM). Data Reduction Computer Program. NASA CR-132656, 1975.

12. Maslowe, S. A.; and Benson, J. L.: Computer Program for the Design and Analysis of Hypersonic Inlets – Final Report. Rep. No. 18079 (Contract No. NAS 2-1460), Lockheed-California Co., Aug. 31, 1964. (Available as NASA CR-77749.)

13. Wyatt, DeMarquis D.: Analysis of Errors Introduced by Several Methods of Weighting Nonuniform Duct Flows. NACA TN 3400, 1955.

14. Jackson, Robert J.; and Wang, Tennyson, T.: Hypersonic Ramjet Experiment Project – Phase I. Computer Program Description Ramjet and Scramjet Cycle Performance. NASA CR-132454, 1974.

15. Andrews, Earl H., Jr.; Mackley, Ernest A.; and Engineering Staff of AiResearch Manufacturing Co.: Hypersonic Research Engines/Aerothermodynamic Integration Model – Experimental Results.
Volume I – Mach 6 Component Integration. NASA TM X-72821, 1976.
Volume II – Mach 6 Performance. NASA TM X-72822, 1976.
Volume III – Mach 7 Component Integration and Performance. NASA TM X-72823, 1976.
Volume IV – Mach 5 Component Integration and Performance. NASA TM X-72824, 1976.

16. Engineering Staff: Hypersonic Research Engine Project – Phase IIA. Aerodynamic and Engine Performance Analysis. Second Interim Technical Data Report. AP-67-3133 (Contract No. NAS1-6666), AiResearch Manufacturing Co., Feb. 13, 1968. (Available as NASA CR-132327.)

17. Andrews, Earl H., Jr.; McClinton, Charles R.; and Pinckney, S. Z.: Flow Field and Starting Characteristics of an Axisymmetric Mixed Compression Inlet. NASA TM X-2072, 1971.

18. Mitchell, Glenn A.; and Cubbison, Robert W.: An Experimental Investigation of the Restart Area Ratio of a Mach 3.0 Axisymmetric Mixed Compression Inlet. NASA TM X-1547, 1968.

19. Ramjet Preliminary Design Report – Conceptual and Preliminary Design of the Hypersonic Ramjet. R66FPD70 (Contract No. NAS1-5115), Adv. Engine Technol. Dep., General Electric Co., Feb. 28, 1966. (Available as NASA CR-66220.)

20. Trexler, Carl A.: Inlet Performance of the Integrated Langley Scramjet Module (Mach 2.3 to 7.6). AIAA Paper No. 75-1212, Sept.-Oct. 1975.

21. Spalding, D. B.; and Chi, S. W.: The Drag of a Compressible Turbulent Boundary Layer on a Smooth Flat Plate With and Without Heat Transfer. J. Fluid Mech., vol. 18, pt. 1, Jan. 1964, pp. 117-143.

TABLE I.- HRE-AIM TEST CONDITIONS AND PERFORMANCE RESULTS

(a) Experimental steady-state flow test cases with no fuel injection

Test case	Corresponding theoretical case (a)	Reading number (b)	Time, sec (b)	M_∞	α, deg	X_C	$\frac{\dot{m}}{\dot{m}_\infty}$	$p_{t,\infty}$		$T_{t,\infty}$		N_{Re}	Performance, force-momentum derived		
								atm	psia	K	°R		M_{th}	η_R	η_{KE}
1		93	134.03	5.146	0	3.904	0.866	28.23	415	1126	2026	3.93×10^6	2.038	0.4356	0.9315
2	9	94	134.14	5.128	0	3.902	.867	29.03	427	1222	2200	3.62	2.051	.4370	.9323
3	9A	95	241.15	5.089	0	3.904	.866	20.39	300	1636	2945	1.94	2.063	.3990	.9120
4		96	134.44	5.061	3	3.914	.813	28.82	424	1231	2216	3.67	1.939	.3782	.9188
5		96	294.64	5.075	3	3.914	.812	28.37	417	1237	2227	3.57	1.941	.3775	.9151
6		97	135.71	5.161	0	3.905	.865	14.35	211	1165	2097	1.91	2.022	.4308	.9270
7	11	60	155.69	6.022	0	3.911	.986	50.78	747	1639	2950	2.38	2.457	.3658	.9444
8	13	61	178.86	5.960	0	4.075	.782	50.65	745	1666	2998	2.33	2.429	.4123	.9469
9	15	61	231.06	5.932	0	4.163	.497	50.71	746	1658	2985	2.33	2.276	.2894	.9121
10		63	186.15	6.010	0	3.906	.984	62.86	924	1677	3019	2.89	2.496	.3853	.9461
11		63	249.15	6.033	0	3.907	.986	32.18	473	1660	2988	1.50	2.546	.4011	.9363
12		64	156.11	6.025	0	3.907	.988	50.88	748	1642	2956	2.40	2.494	.3805	.9456
13		65	164.03	6.015	0	3.909	.981	51.02	750	1686	3035	2.33	2.530	.4005	.9455
14		69	175.20	6.013	0	3.905	.986	51.02	750	1667	3001	2.35	2.467	.3715	.9418
15		71	160.54	6.016	3	3.907	.933	50.54	743	1609	2897	2.44	2.149	.2497	.9196
16		88	236.40	7.125	0	4.065	.989	68.03	1000	1754	3157	1.64	2.816	.3215	.9398
17		89	250.77	7.381	0	4.063	.991	67.28	989	996	1794	4.75	2.833	.3228	.9396
18	23A	90	197.22	7.144	0	4.063	.991	67.71	996	1662	2992	1.81	2.820	.3230	.9413
19		91	186.45	7.167	3	4.061	.904	67.64	995	1705	3069	1.80	2.537	.2152	.9063
20		92	186.87	7.381	0	4.061	.993	67.55	993	1141	2053	3.63	2.807	.3203	.9475
												Average			[c] 0.937

(b) Theoretical computer program cases

[$\alpha = 0^0$]

Theoretical case (a)	M_∞	X_C	$\frac{\dot{m}}{\dot{m}_\infty}$	$\frac{h_{t,th}}{h_{t,\infty}}$	δ_{th}/h'		δ^*_{th}/h'		$p_{t,\infty}$		$T_{t,\infty}$		$\frac{p_{th}}{p_\infty}$	Performance					
														Mass-weighted average			Force-momentum derived		
					Spike	Cowl	Spike	Cowl	atm	psia	K	°R		M_{th}	η_R	η_{KE}	M_{th}	η_R	η_{KE}
9	5.15	3.920	0.845	0.977	0.2266	0.1591	0.0544	0.0344	14.08	207	1248	2245	23.741	2.554	0.6180	0.9360	2.132	0.4728	0.9249
[d] 9A	5.15	3.920	.882	.984	.2458	.1707	.0657	.0495	20.39	300	1667	3000	18.383	2.608	.5692	.9435			
11	6.00	3.907	.986	.974	.2218	.1338	.0531	.0270	63.22	930	1628	2930	27.060	2.976	.5875	.9345	----	-----	-----
13	6.00	4.066	.803	.976	.2106	.0642	.0508	.0106	63.22	930	1628	2930	42.148	2.777	.6146	.9454			
15	6.00	4.120	.665	.973	.2321	.1120	.0564	.0174	63.22	930	1628	2930	38.213	2.654	.4621	.9243			
[d] 23A	7.25	4.058	1.000	.970	.2134	.0873	.0624	.0161	68.00	1000	1667	3000	60.142	3.106	.4428	.9386	2.622	.2610	.9310
													Average			0.937			0.928

[a] Corresponds to case numbers in reference 1.

[b] Corresponds to case identification in reference 15.

[c] Only cases for $\alpha = 0^0$ have been averaged.

[d] Recomputed cases which correspond more closely to AIM test conditions.

TABLE II.- HRE-AIM INLET COORDINATES AND RADIAL ANGLES

USED IN THE PRESENT AIM THEORETICAL ANALYSIS

[Mach 6 design cowl position, $X_C = 3.872$]

(a) Spike

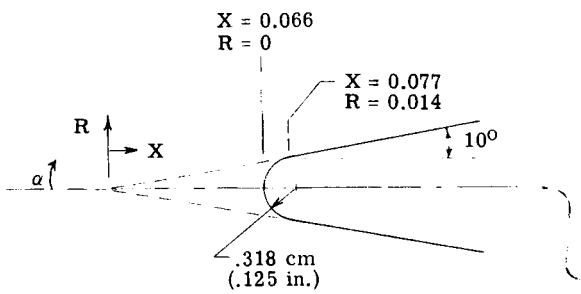

(b) Cowl

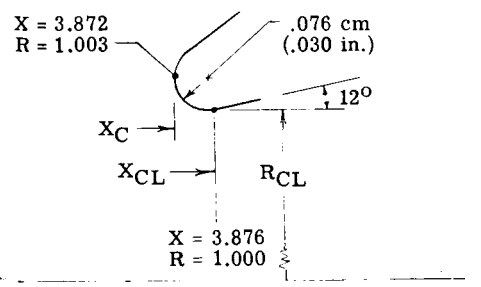

X	R	
0.066	0.0	
.077	.014	Straight line
2.040	.360	$\xi = 10.0^\circ$
2.145	.379	
2.271	.404	
2.410	.432	
2.537	.458	
2.650	.482	
2.875	.531	
2.974	.554	
3.100	.584	
3.212	.613	
3.295	.636	Straight line
3.373	.658	$\xi = 15.819^\circ$
3.640	.740	
3.787	.793	Straight line
4.190	.956	$\xi = 22.0^\circ$
4.230	.971	
4.274	.984	
4.308	.991	
4.341	.997	
4.374	1.003	
4.408	1.087	
4.411	1.013	
4.500	1.020	Throat
4.602	1.030	
4.659	1.035	
4.714	1.040	

X	R	
3.872	1.003	$\xi = 90^\circ$
3.876	1.0	$\xi = 12^\circ$
3.933	1.012	
3.986	1.021	$\xi = 10^\circ$
4.019	1.027	
4.046	1.031	$\xi = 8^\circ$
4.085	1.036	
4.166	1.044	Straight line
5.326	1.159	$\xi = 5.645^\circ$

(c) Radial angles (looking downstream)

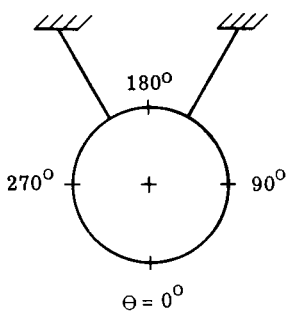

TABLE III.- COMBUSTOR CONFIGURATION AND FUEL INJECTOR PARAMETERS

[Mach 6 design cowl position, $X_C = 3.872$]

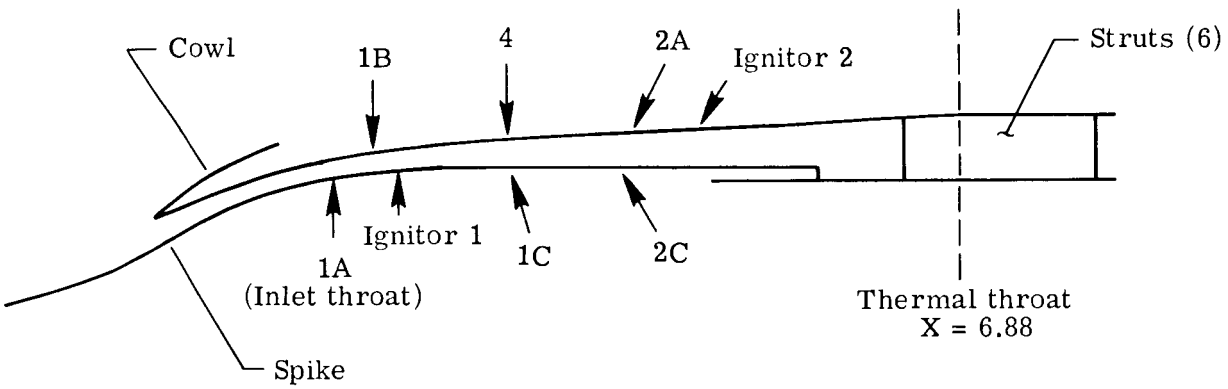

Designation (a)	Number of injectors	Orifice diameter, d, cm (in.)	Injection angle, deg (b)	Peripheral spacing, s/d	X-location
Fuel injectors					
1A	37	0.302 (0.119)	90	13.1	4.50
1B	37	.302 (.119)	90	13.9	4.58
1C	37	.302 (.119)	106	13.5	4.94
4	37	.302 (.119)	90	14.2	4.94
2A	60	.241 (.095)	67	11.4	5.39
2C	60	.241 (.095)	119	10.6	5.17
Ignitors					
Ignitor 1	6		94.5	Equally	4.67
Ignitor 2	6		60	spaced	5.66

[a] Designations used in all HRE documentation; see for example, reference 9.

[b] With respect to AIM center line in the view shown in the sketch.

TABLE IV.- GEOMETRIC CHARACTERISTICS OF HRE-AIM AND HRE TWO-DIMENSIONAL COMBUSTORS

Characteristic	Two-dimensional combustor (ref. 10)	AIM (X_C = 3.872)
Duct height, h', cm (in.)	1.85 (0.73)	≈1.30 (≈0.51)
Duct width, cm (in.)	11.43 (4.50)	Annulus with mean radius of 24.0 (9.45)
Longitudinal distance between opposing wall fuel injectors, cm (in.)	1.91 (0.75)	1.91 (0.75)
Number of orifices:		
Fuel injector 1A	2	37
Fuel injector 1B	3	37
Orifice diameter, d, cm (in.)	0.302 (0.119)	0.302 (0.119)
Orifice lateral spacing, s/d (center-to-center):		
Fuel injector 1A	12.6	13.1
Fuel injector 1B	12.6	13.9
Orifices interdigitized	Yes	No
Sidewall effects	Yes	No

TABLE V.- LOCATIONS OF STATIC-PRESSURE ORIFICES IN HRE-AIM INLET

[Mach 6 design cowl position, $X_C = 3.872$]

(a) Spike

X	θ, deg
0.066	--- Spike tip
[a] 1.600	0
[a] 1.600	90
[b] 1.600	180
1.600	271
3.400	0
3.889	0
3.889	90
3.889	180
3.889	270
3.944	0
4.000	0
4.056	0
4.056	89
4.056	180
4.056	269
4.111	0
[a] 4.222	0
[a] 4.222	90
[a] 4.222	180
4.222	269
4.333	0
[a] 4.333	180
[a] 4.333	269
4.389	0
4.444	0
4.444	89
4.444	180
4.444	269
4.611	0
4.722	0

(b) Cowl

X	θ, deg
3.944	0
[b] 4.000	0
[b] 4.056	0
[b] 4.056	180
4.111	0
4.111	90
[a] 4.111	180
[a] 4.111	270
[b] 4.167	0
4.222	0
4.222	90
[b] 4.222	180
[a] 4.222	270
4.278	0
4.333	0
4.333	90
[a] 4.333	180
[b] 4.333	270
4.389	359
[b] 4.444	0
[a] 4.444	90
4.444	180
[a] 4.444	270
[b] 4.567	0
4.567	180
4.567	210
4.567	330

[a] Deleted because of instrumentation channel limitation.

[b] Deleted because of instrumentation malfunction.

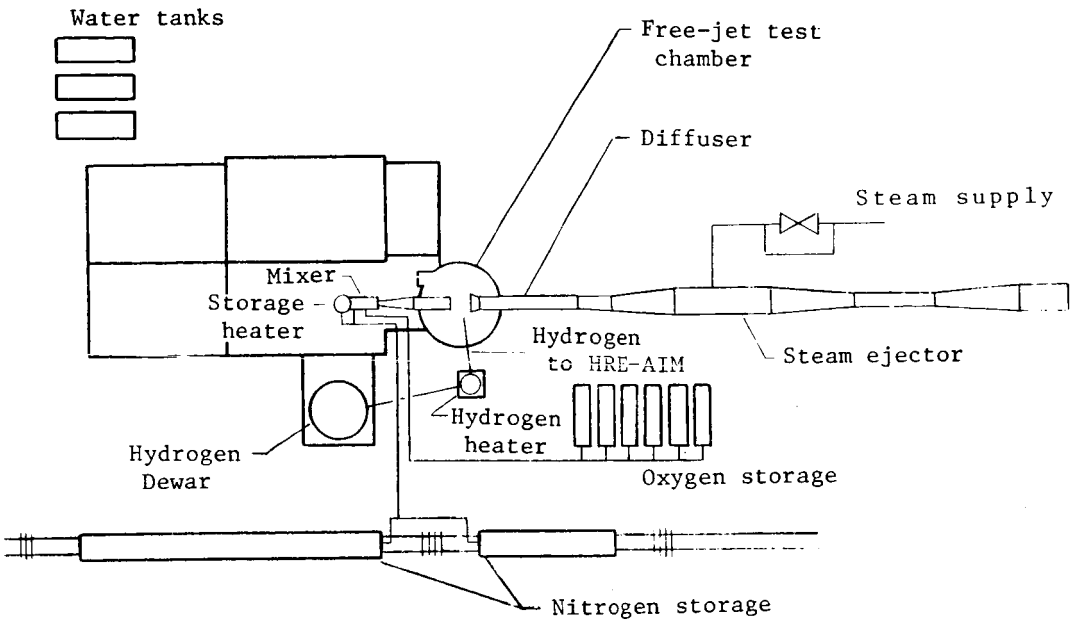

(a) Schematic layout of HTF.

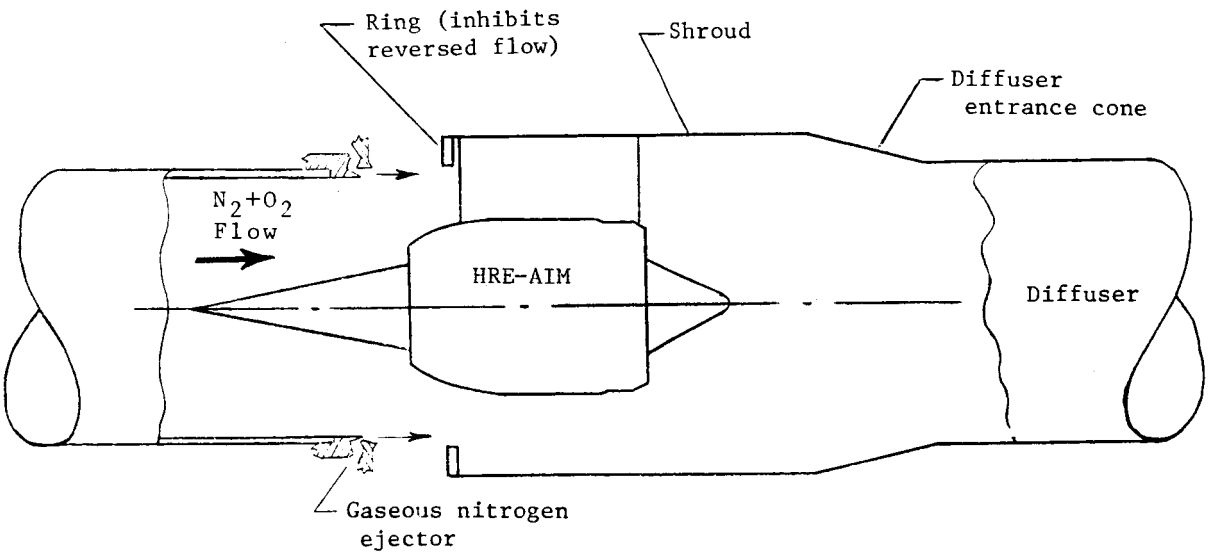

(b) Schematic of HRE-AIM located in free-jet test chamber of HTF.

Figure 1.- Lewis Hypersonic tunnel facility (HTF).

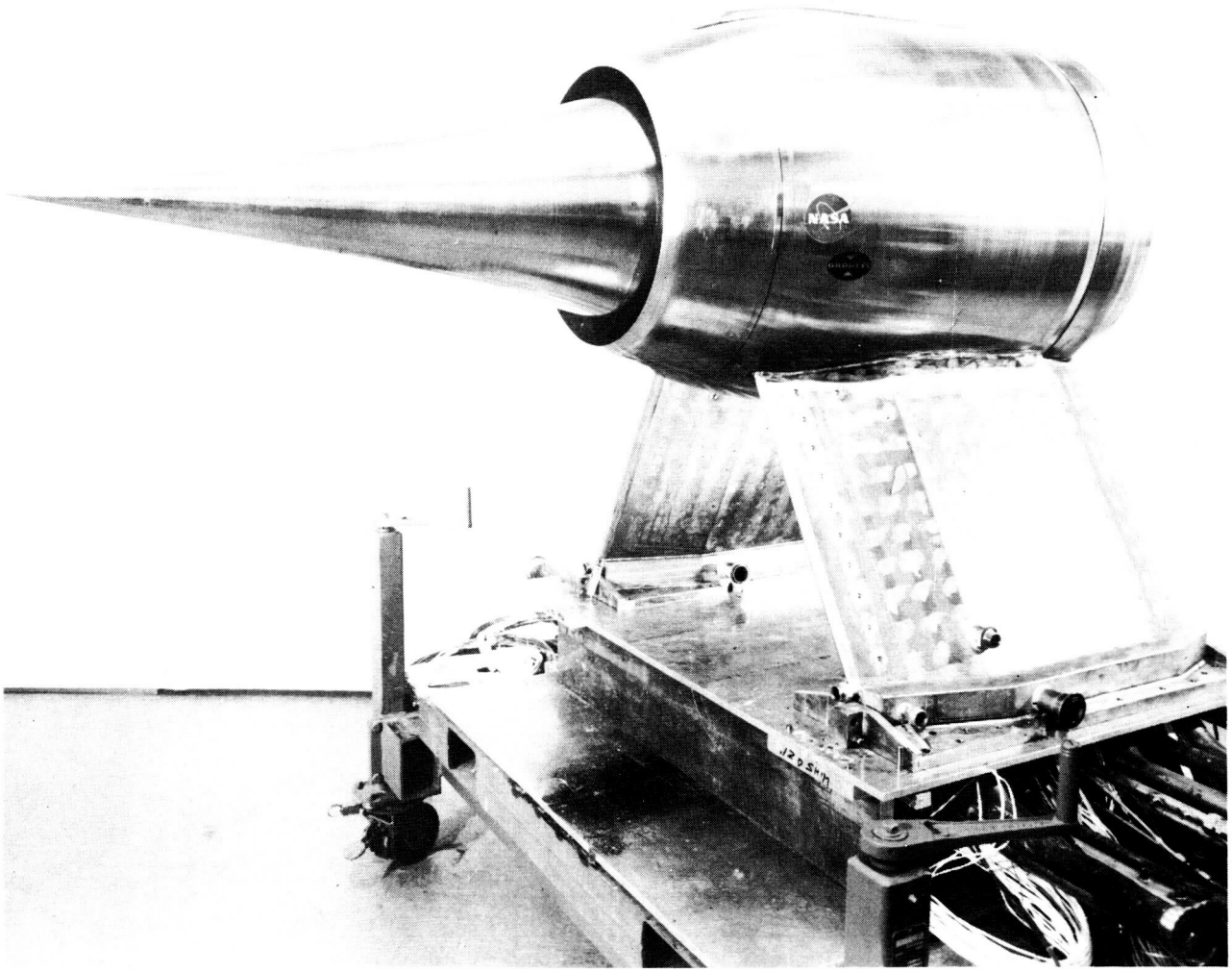

(a) Pretest photograph of HRE-AIM. (AiResearch Manufacturing Co. photograph.)

Figure 2.- Hypersonic Research Engine (HRE) Aerothermodynamic Integration Model (AIM).

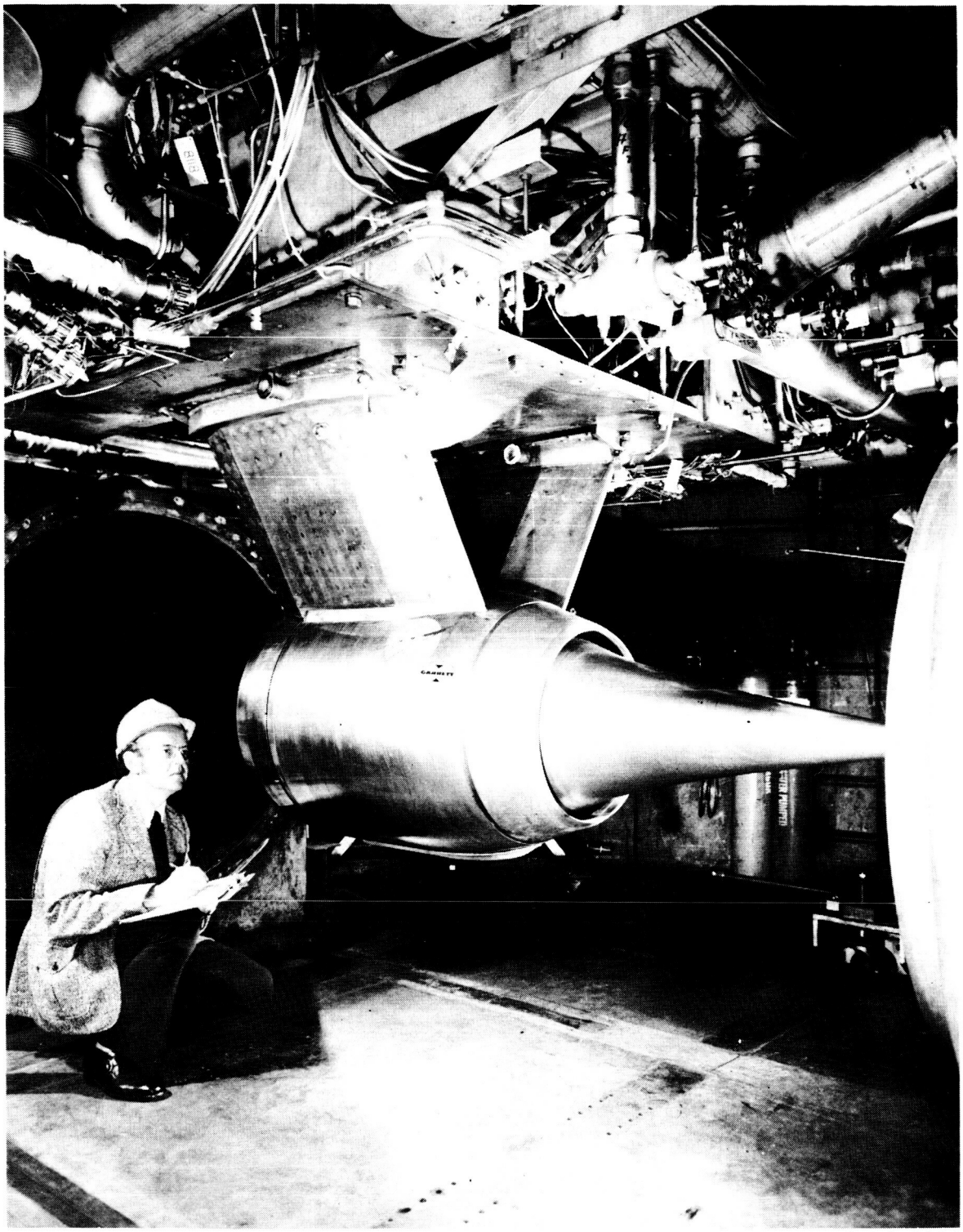

C-73-2624

(b) HRE-AIM partially installed in HTF.

Figure 2.- Continued.

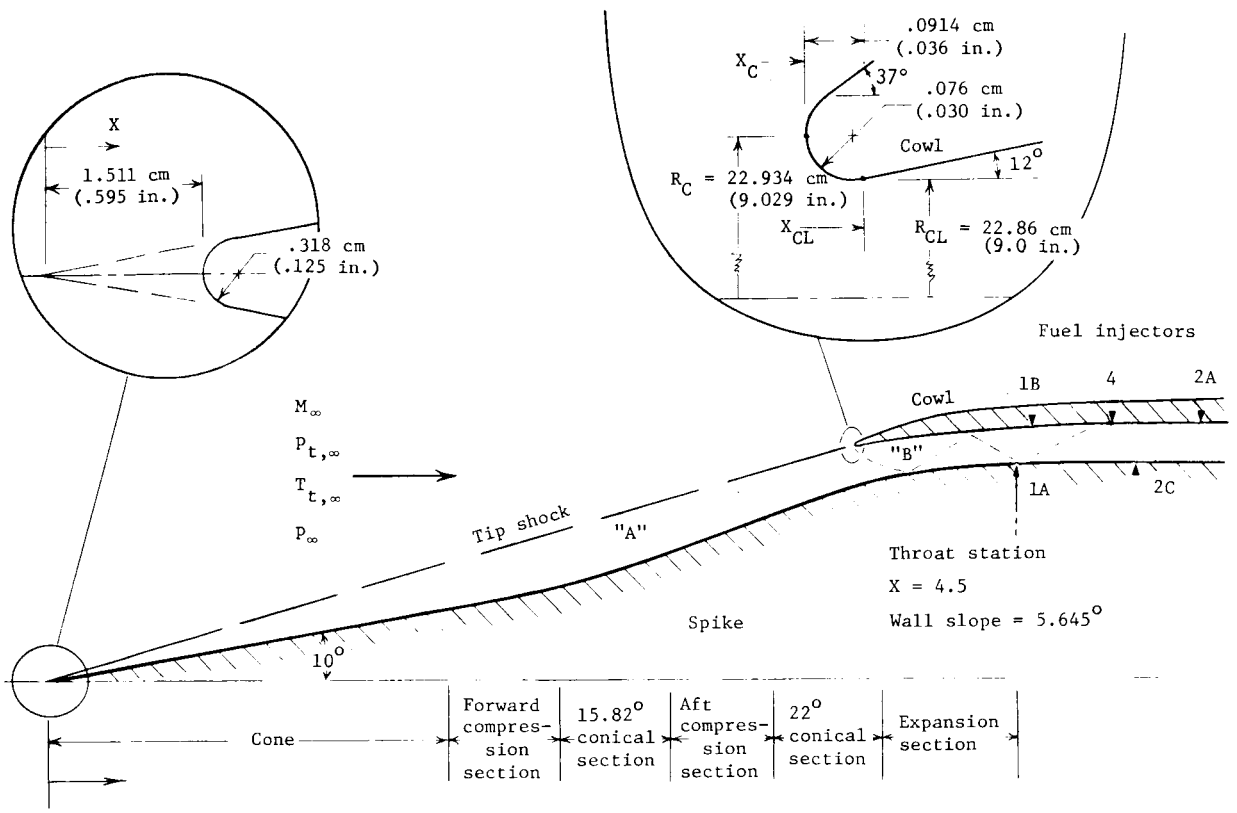

M_∞	X_C	Fuel injector X-locations for —			
		First stage		Second stage	
		1A	1B or 4	2A	2C
5.15	3.91	4.50	4.58 or 5.18	5.62	5.14
6.05	3.91	4.50	4.58 or 5.18	5.62	5.14
7.25	4.06	4.50	4.74 or 5.34	5.78	5.14

(c) AIM inlet schematic.

Figure 2.- Concluded.

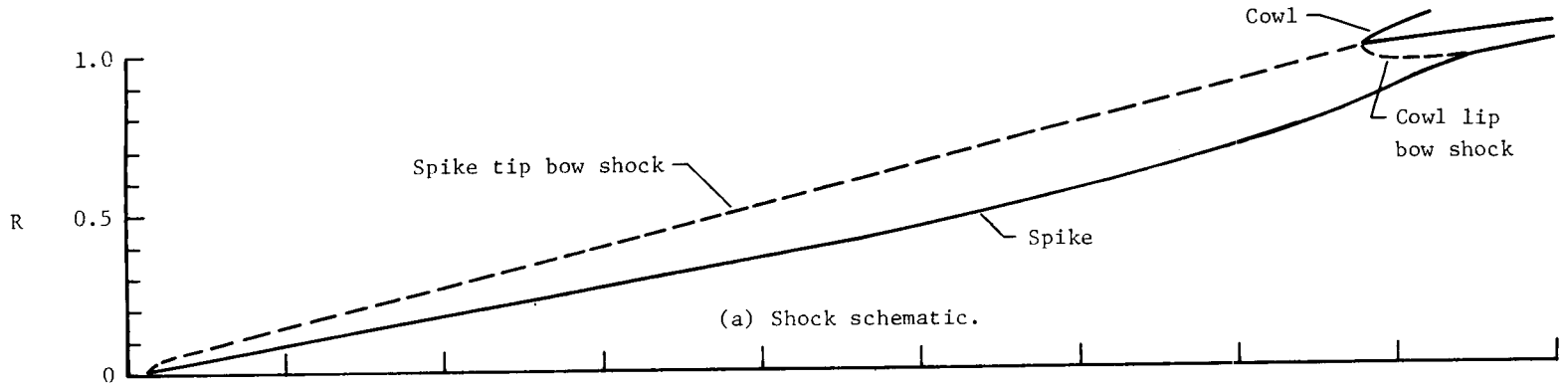

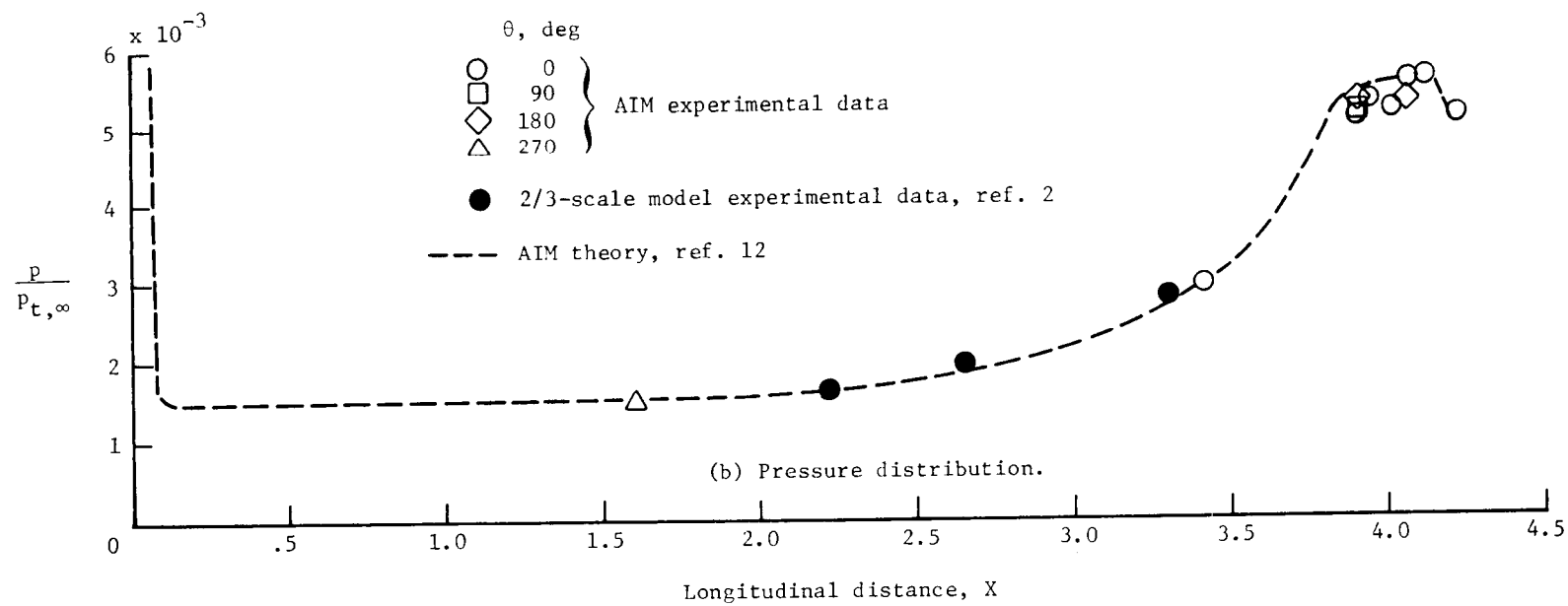

Figure 3.- Typical spike surface-pressure distributions. $M_\infty \approx 6.05$; $\alpha = 0^o$.

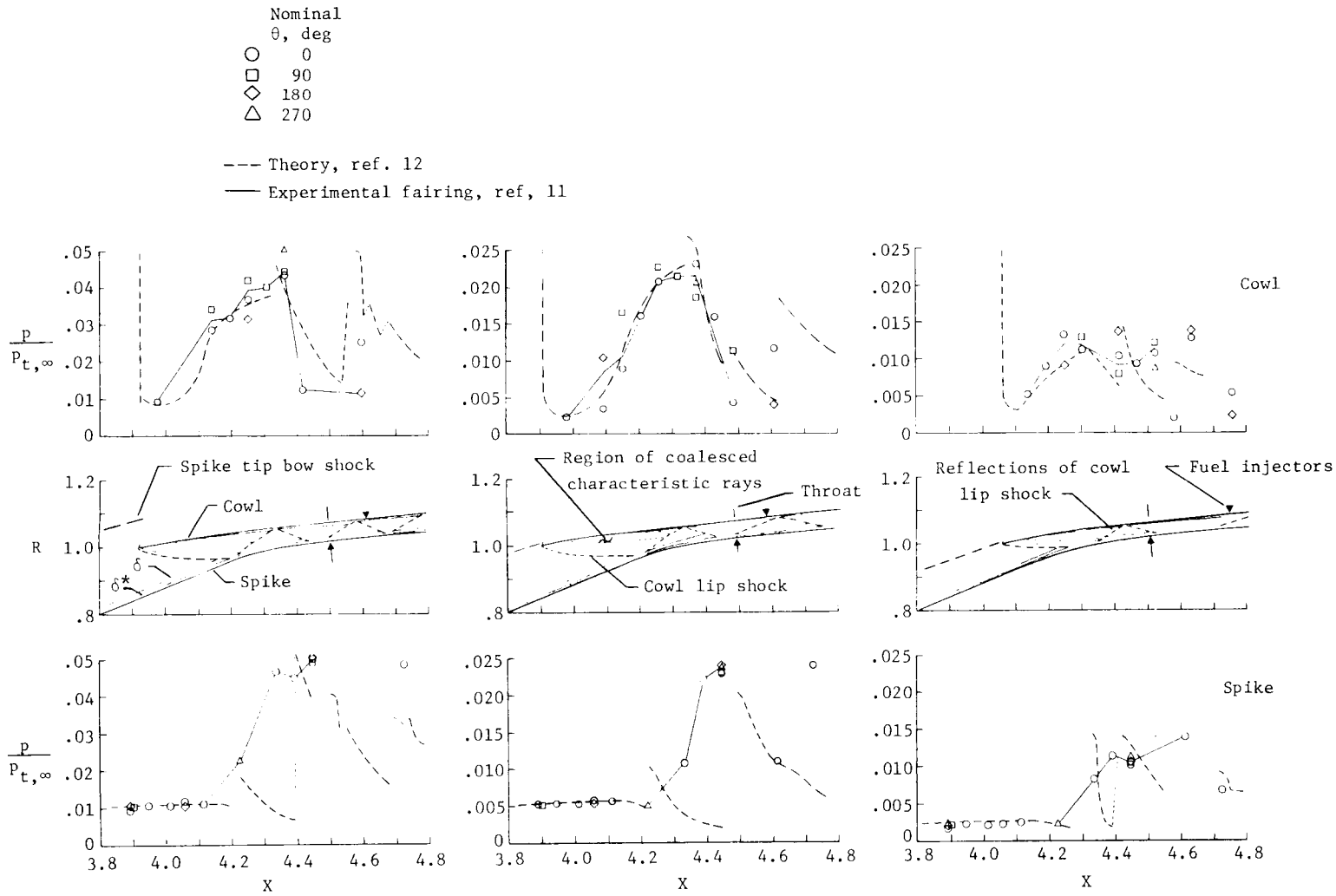

(a) M ≈ 5.15; test case 2; theoretical case 9.

(b) M ≈ 6.05; test case 7; theoretical case 11.

(c) M ≈ 7.25; test case 18; theoretical case 23A.

Figure 4.- Effect of free-stream Mach number on inlet internal flow. $\alpha = 0^{o}$.

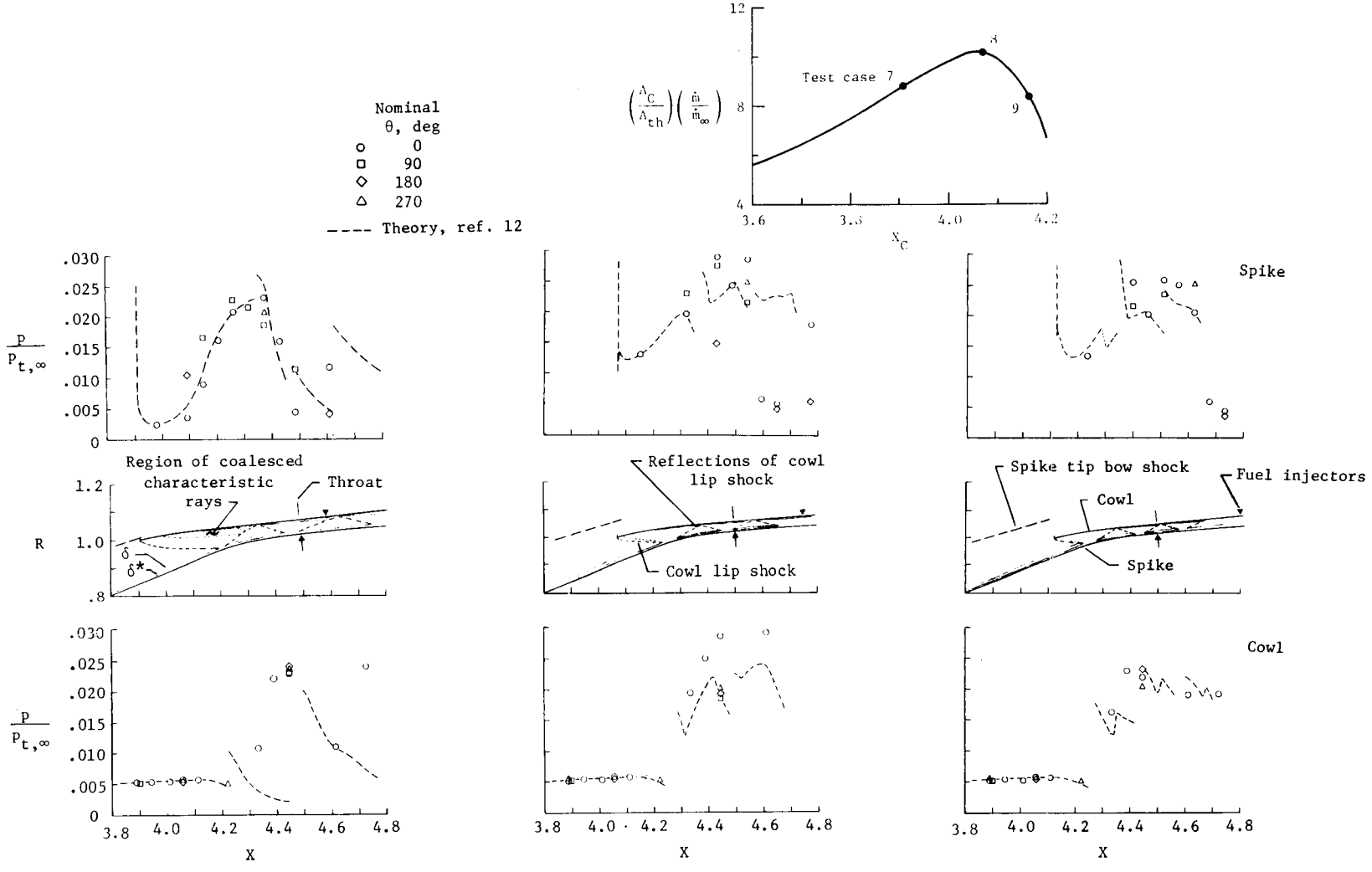

(a) $X_C = 3.911$; $\frac{\dot{m}}{\dot{m}_\infty} \approx 1.0$; $\left(\frac{A_C}{A_{th}}\right)\left(\frac{\dot{m}}{\dot{m}_\infty}\right) \approx 8.85$; test case 7; theoretical case 11.

(b) $X_C = 4.075$; $\frac{\dot{m}}{\dot{m}_\infty} \approx 0.8$; $\left(\frac{A_C}{A_{th}}\right)\left(\frac{\dot{m}}{\dot{m}_\infty}\right) \approx 10.1$; test case 8; theoretical case 13.

(c) $X_C = 4.163$; $\frac{\dot{m}}{\dot{m}_\infty} \approx 0.5$; $\left(\frac{A_C}{A_{th}}\right)\left(\frac{\dot{m}}{\dot{m}_\infty}\right) \approx 8.45$; test case 9; theoretical case 15.

Figure 5.- Effect of cowl position on inlet internal flow. $M_\infty \approx 6.05$; $\alpha = 0^o$.

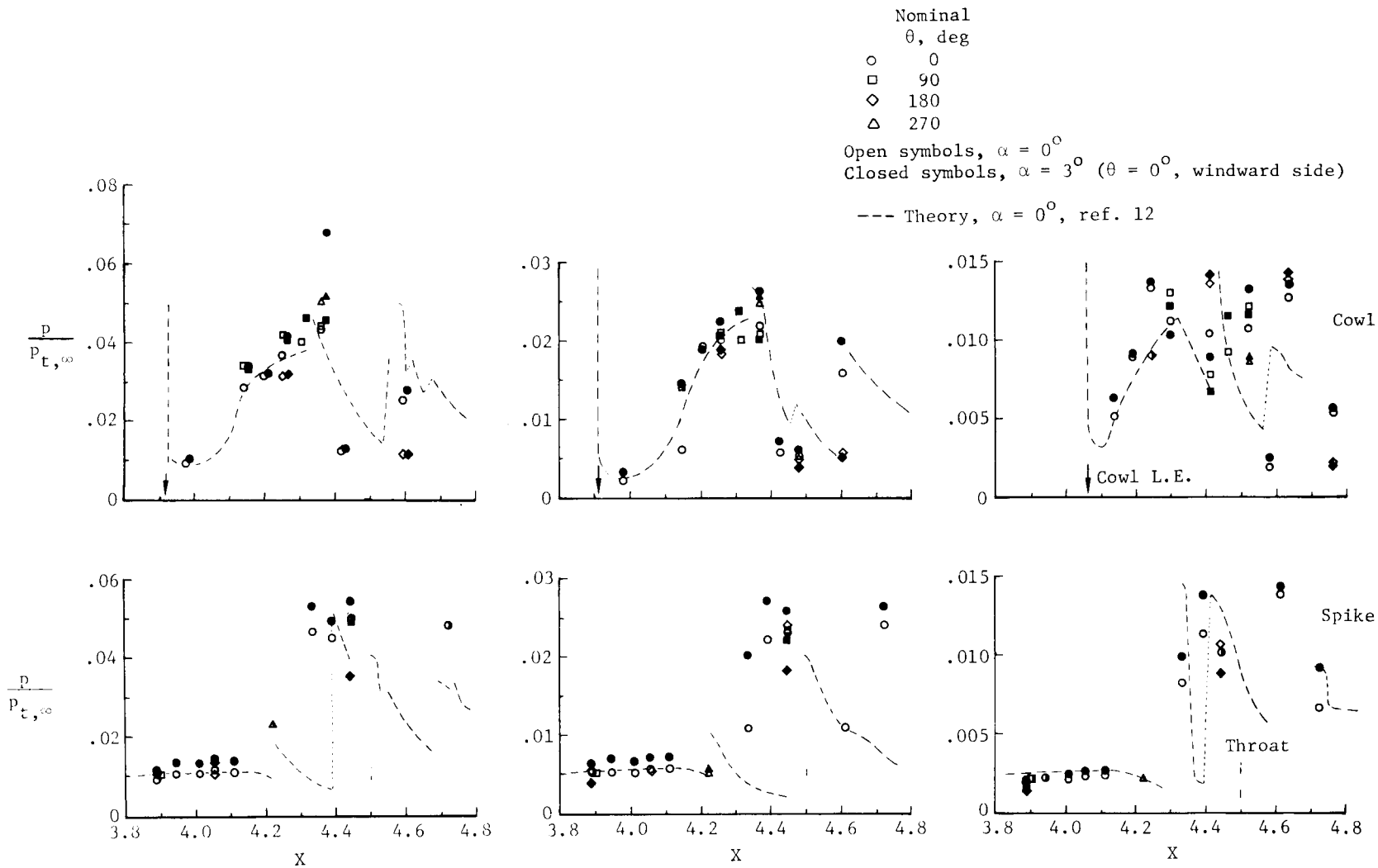

(a) $M_\infty \approx 5.15$; test cases 2 and 4; theoretical case 9.

(b) $M_\infty \approx 6.05$; test cases 7 and 15; theoretical case 11.

(c) $M_\infty \approx 7.25$; test cases 18 and 19; theoretical case 23A.

Figure 6.- Angle-of-attack effect on inlet internal static-pressure distributions.

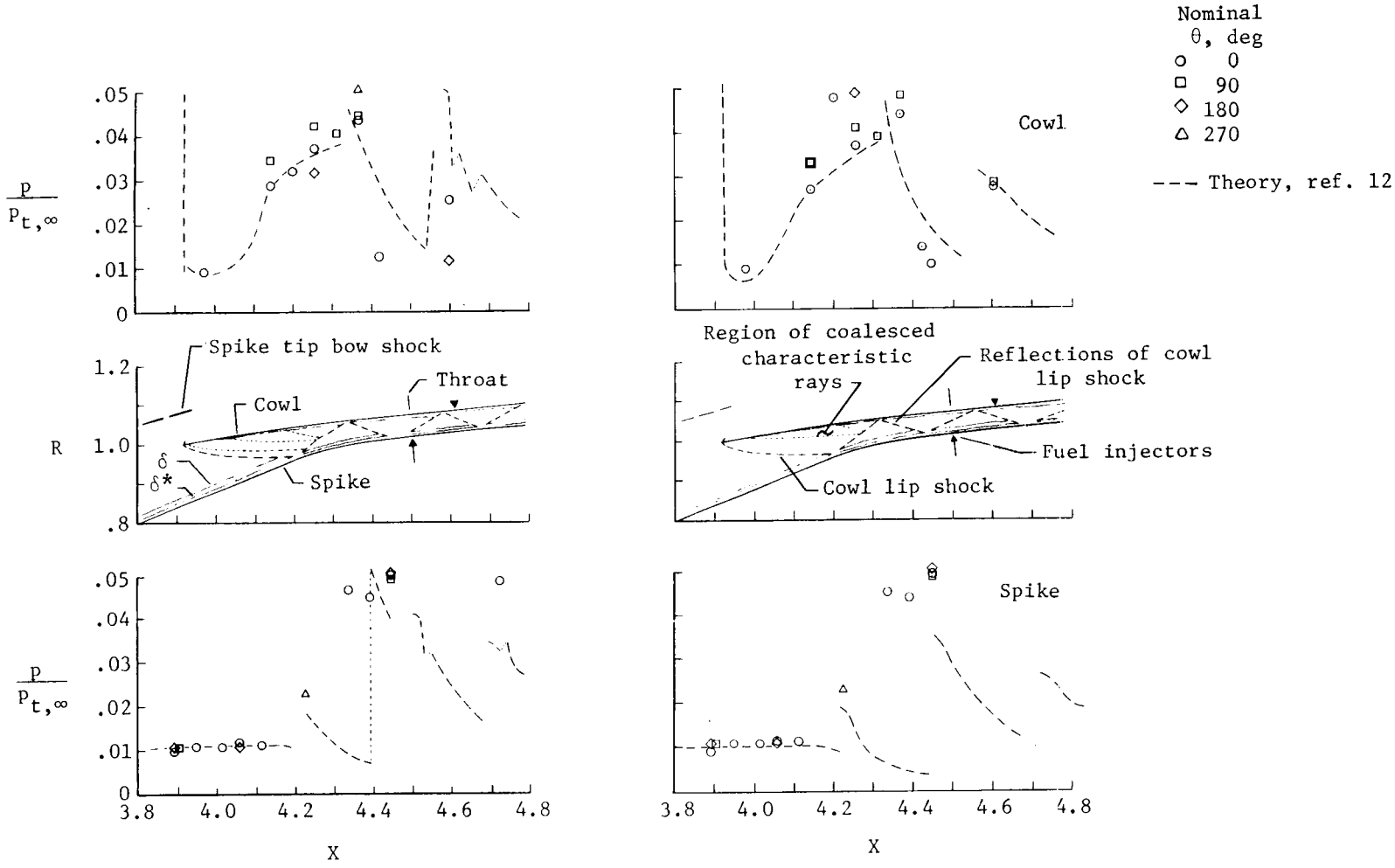

(a) HRE-AIM in free stream. Test case 2; theoretical case 9.

(b) Simulation of HRE-AIM behind bow shock of vehicle having 10° half-angle conical nose in Mach 6 flight. Test case 3; theoretical case 9A.

Figure 7.- Effect of simulated vehicle flow field on inlet internal flow. $M_\infty \approx 5.15$; $\alpha = 0^\circ$.

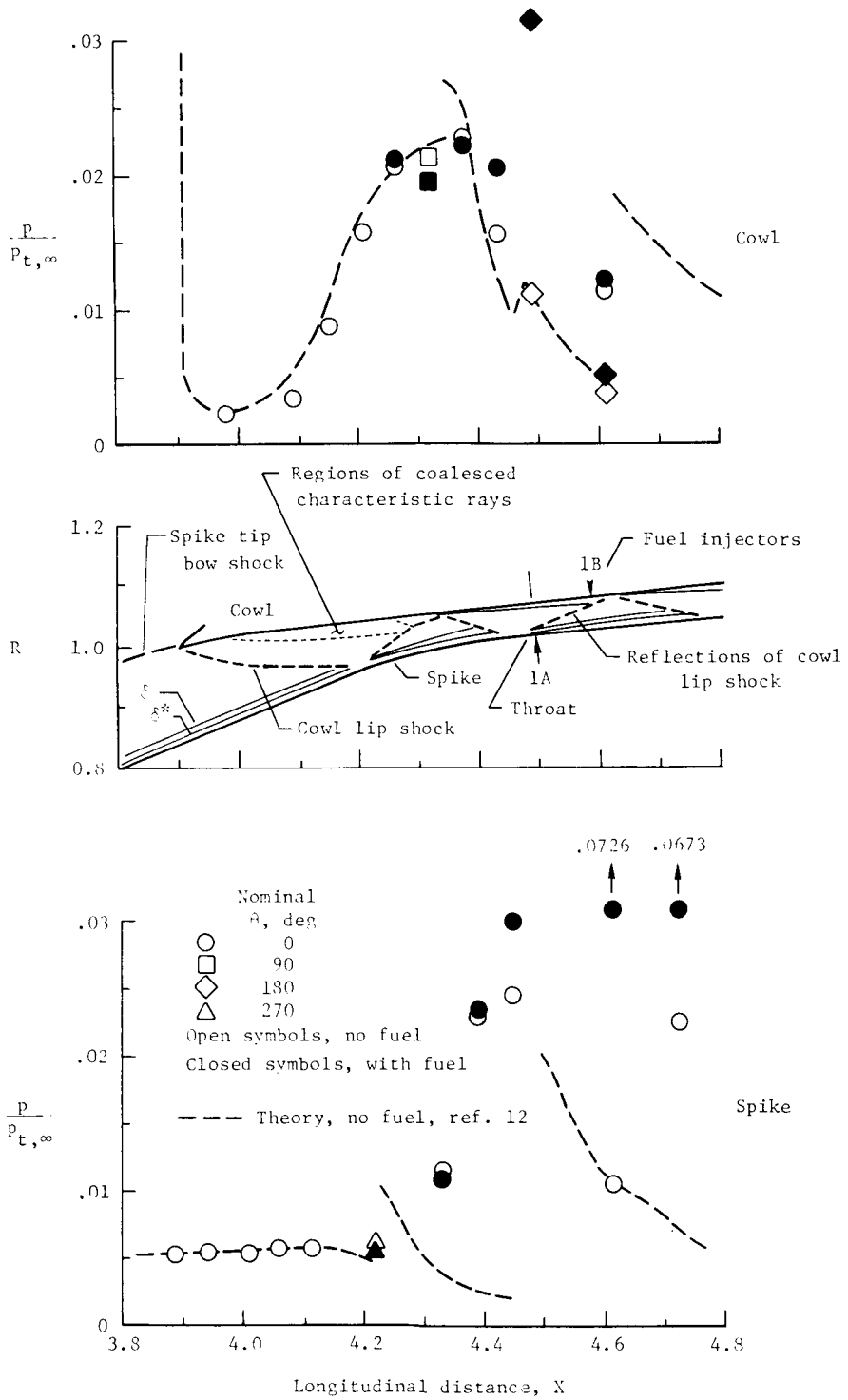

Figure 8.- Effect of inlet-combustor interaction on inlet surface-pressure distributions. $M_\infty \approx 6.05$; $\alpha = 0^o$; for data with fuel $\phi_{tot} = \phi_1 = 0.348$ (just prior to inlet unstart).

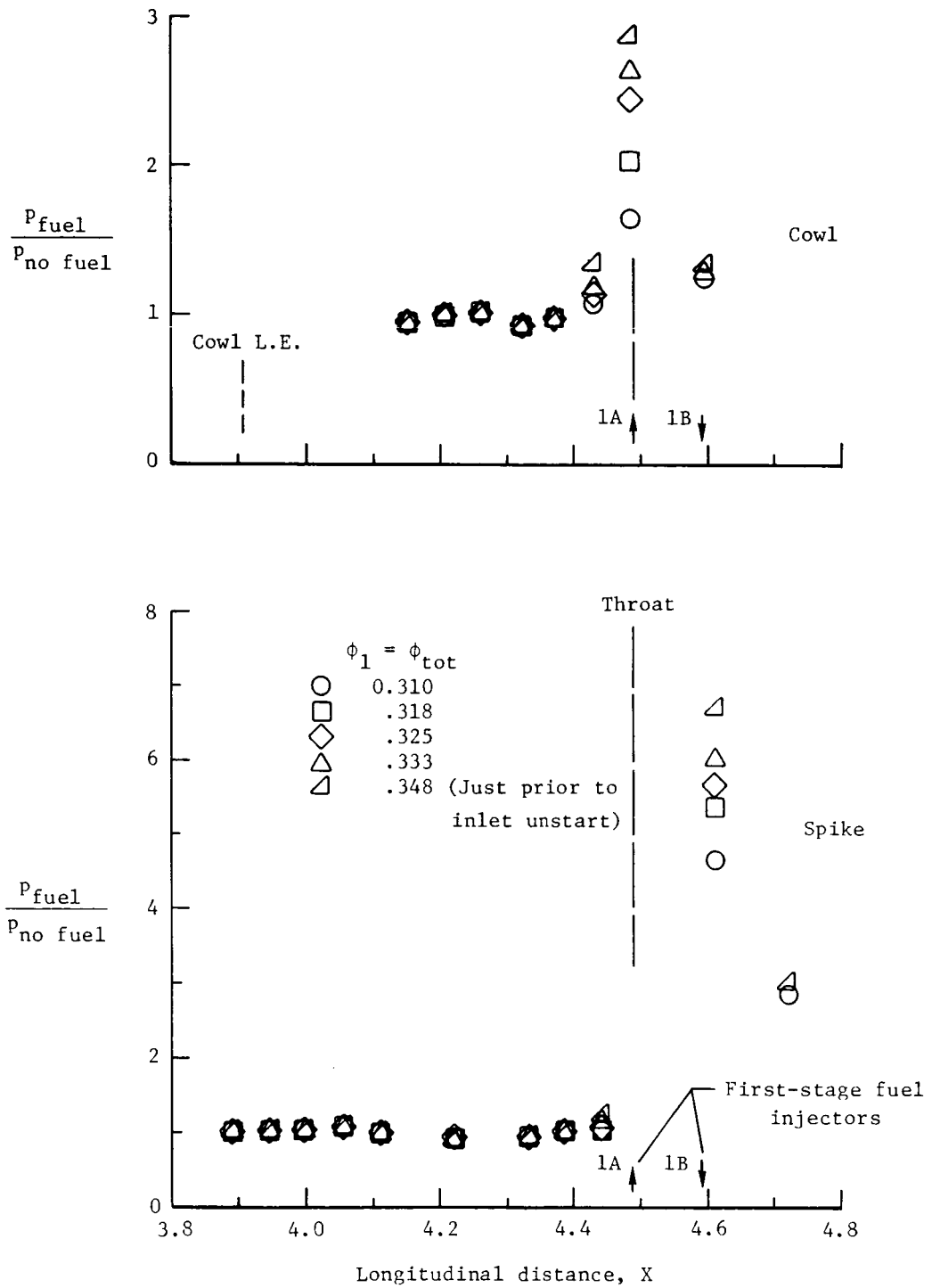

Figure 9.- Inlet surface-pressure increase associated with first-stage fuel injection and combustion. $M_\infty \approx 6.05$; $\alpha = 0^o$.

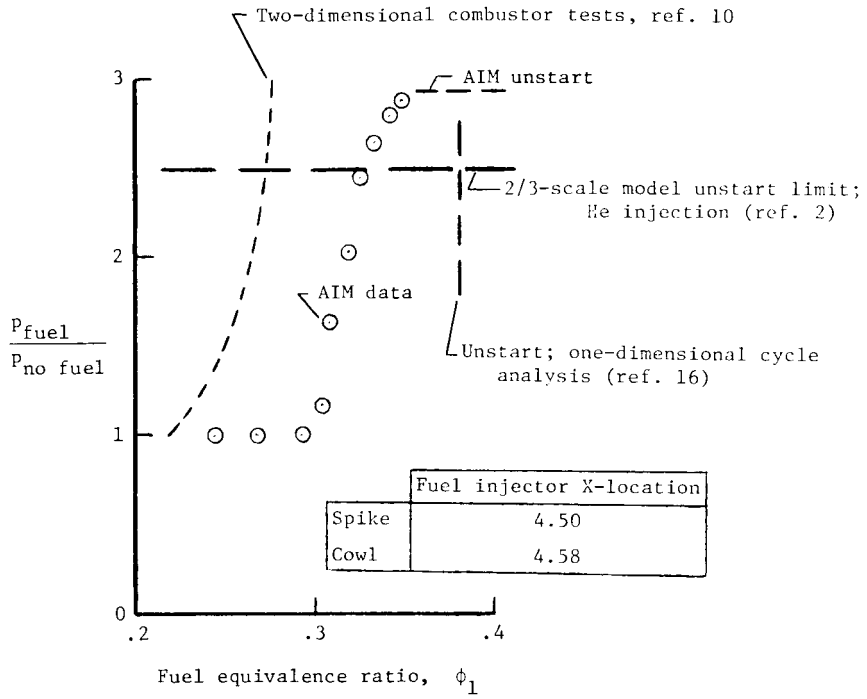

(a) First-stage fuel injection with spike ignitors at $X = 4.66$. $M_\infty \approx 6.05$; measuring station at $X = 4.48$; $X_C = 3.91$; $\theta = 0^o$; $\alpha = 0^o$.

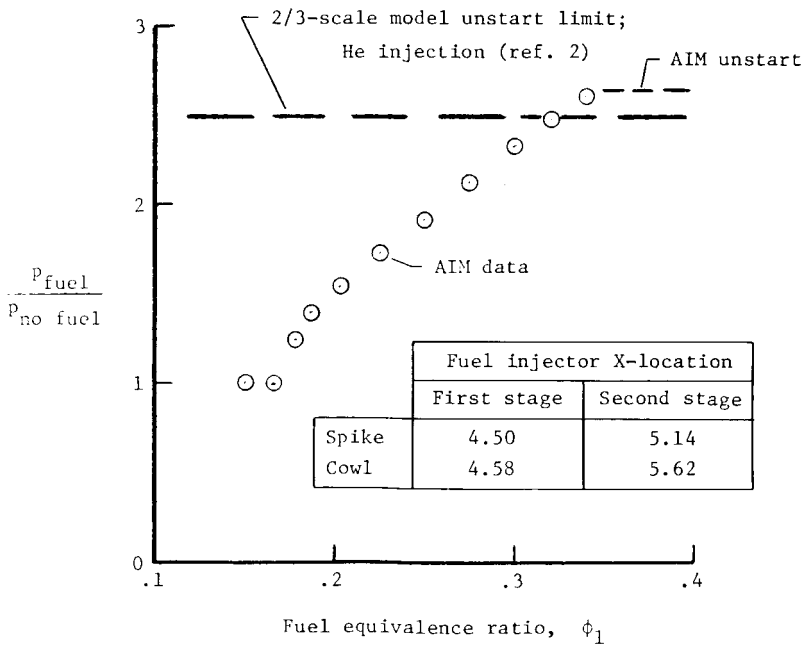

(b) Staged fuel injection with ignition by fuel stage interaction. $M_\infty \approx 6.05$; $\phi_{tot} \approx 0.93$; measuring station at $X = 4.48$; $X_C = 3.91$; $\theta = 0^o$; $\alpha = 0^o$.

Figure 10.- Effects of inlet-combustor interaction on cowl surface throat pressure.

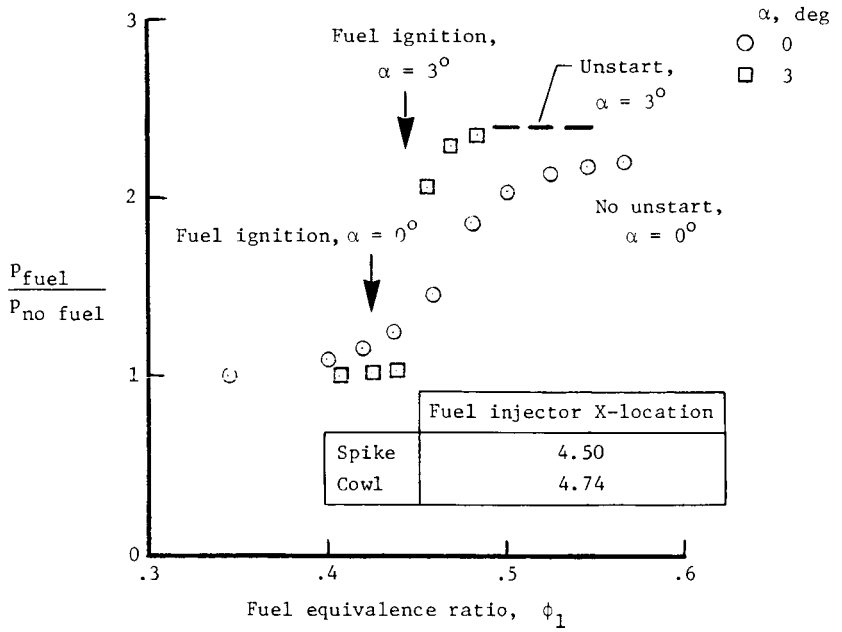

(c) First-stage fuel injection with cowl ignitors at $X = 5.85$. $M_\infty \approx 7.25$; measuring station at $X = 4.52$; $X_C = 4.06$; $\theta = 90^\circ$.

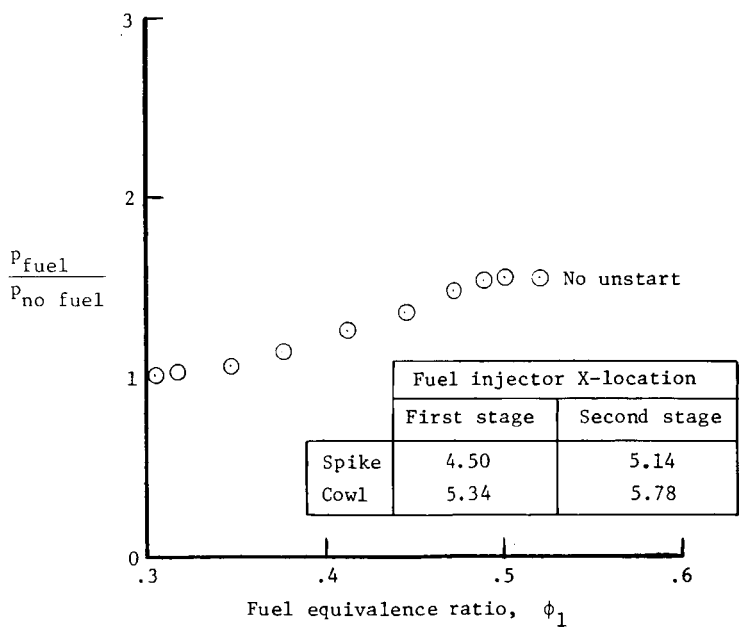

(d) Staged fuel injection with cowl ignitors at $X = 5.85$. $M_\infty \approx 7.25$; $\phi_{tot} \approx 0.95$; measuring station at $X = 4.52$; $X_C = 4.06$; $\theta = 90^\circ$; $\alpha = 0^\circ$.

Figure 10.- Concluded.

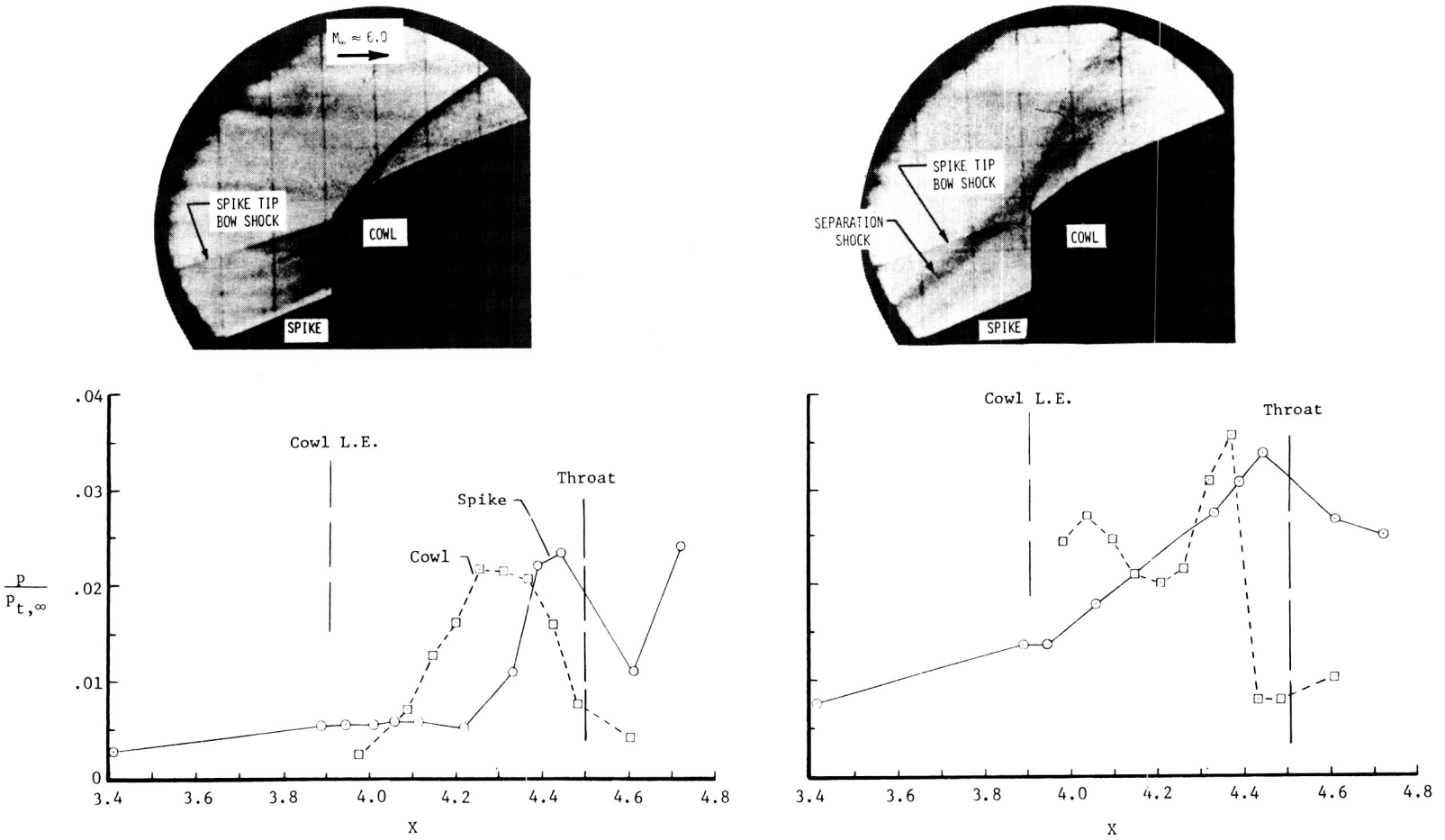

(a) Inlet in start condition. $\phi = 0$.

(b) Inlet in unstarted condition. Unstart occurred at $\phi_1 \approx 0.35$.

Figure 11.- Schlieren photographs and experimental pressure distributions for inlet start and unstart conditions. $M_\infty \approx 6.0$; $\alpha = 0^o$.

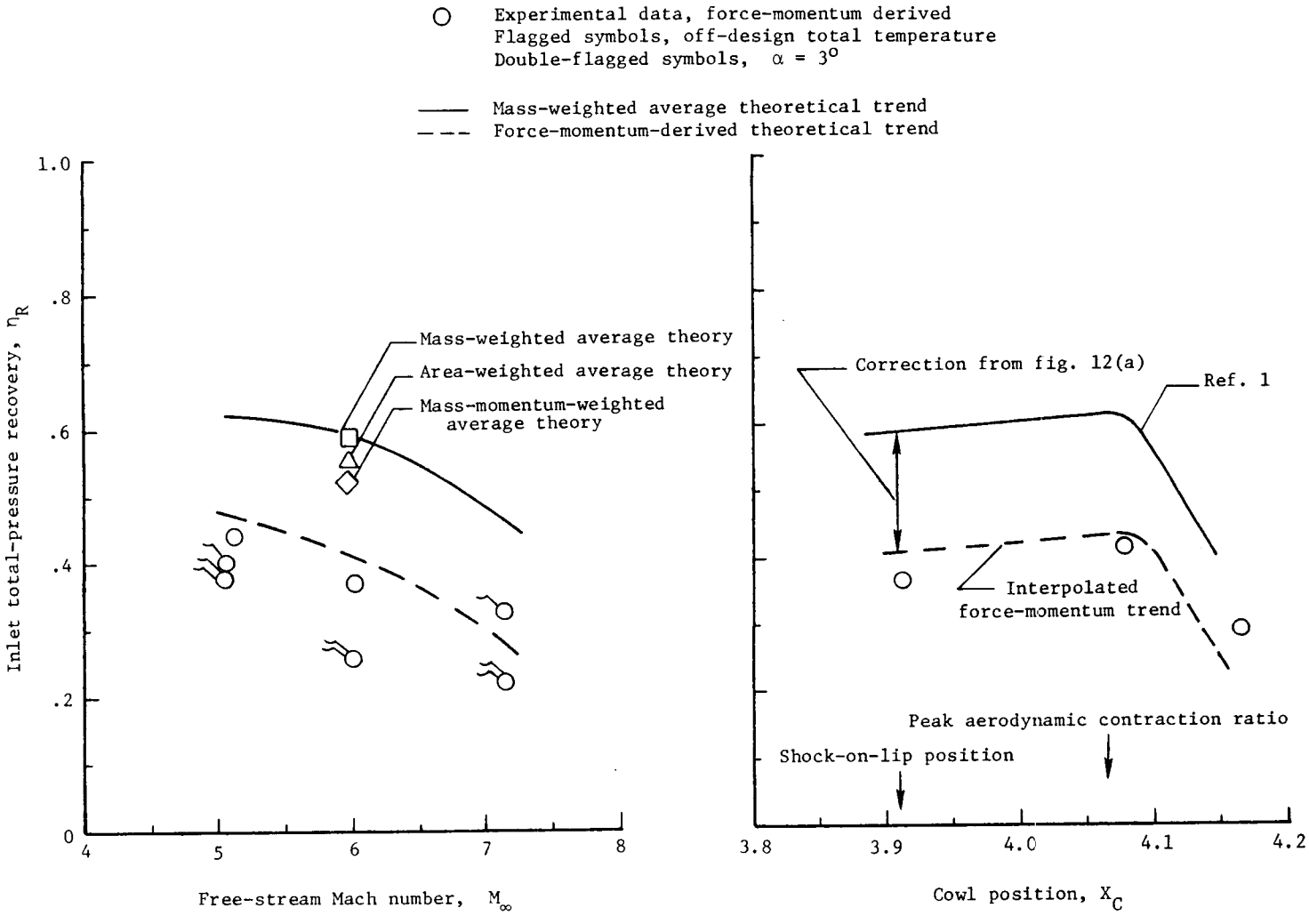

(a) Variation with free-stream Mach number. Design operating cowl positions.

(b) Variation with cowl position. $M_\infty \approx 6.05$.

Figure 12.- HRE-AIM inlet throat total-pressure recovery. $\alpha = 0^\circ$ unless otherwise indicated.

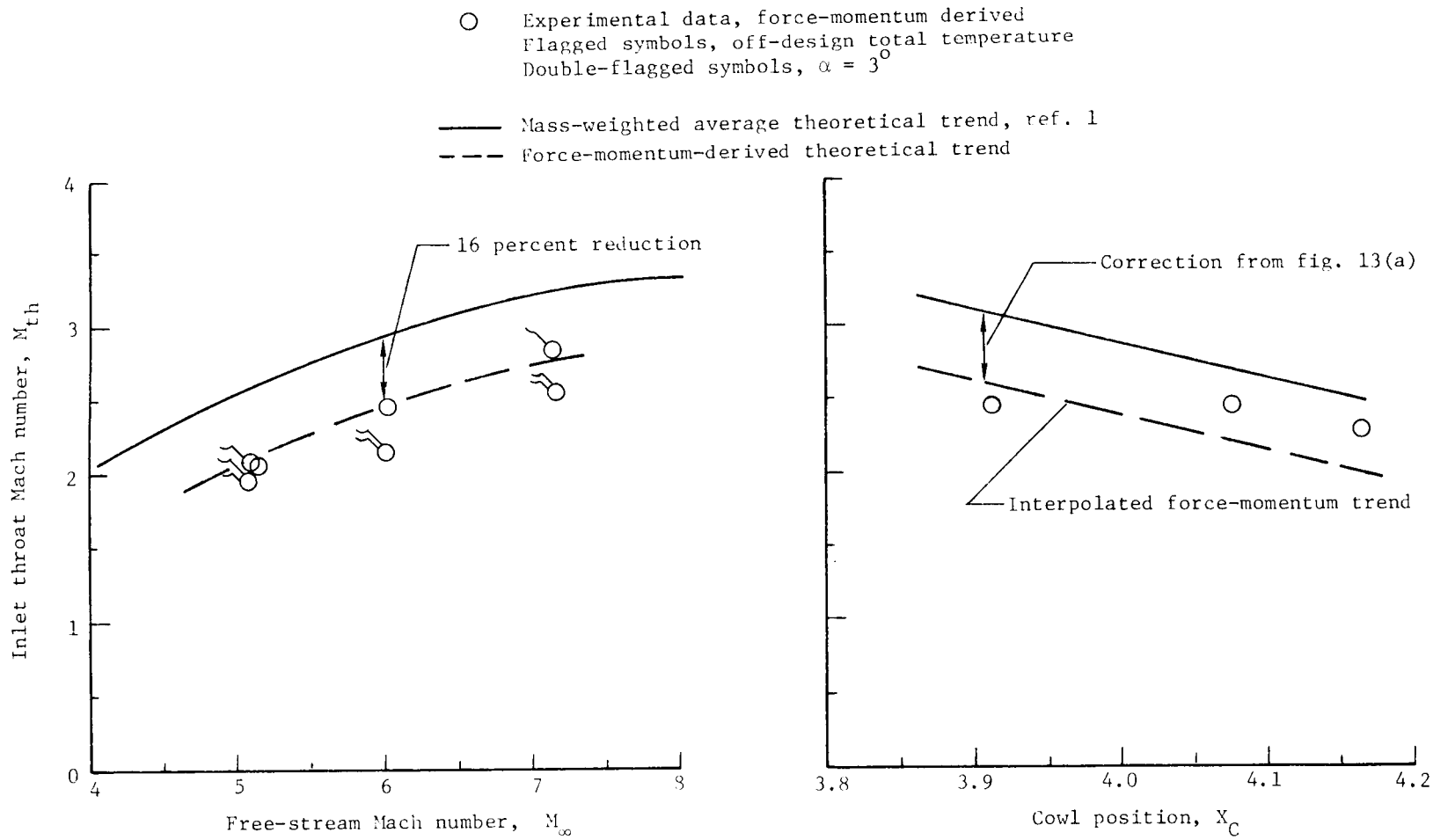

(a) Variation with free-stream Mach number. Design operating cowl positions.

(b) Variation with cowl position. $M_\infty \approx 6.05$.

Figure 13.- HRE-AIM inlet throat Mach number. $\alpha = 0^o$ unless otherwise indicated.

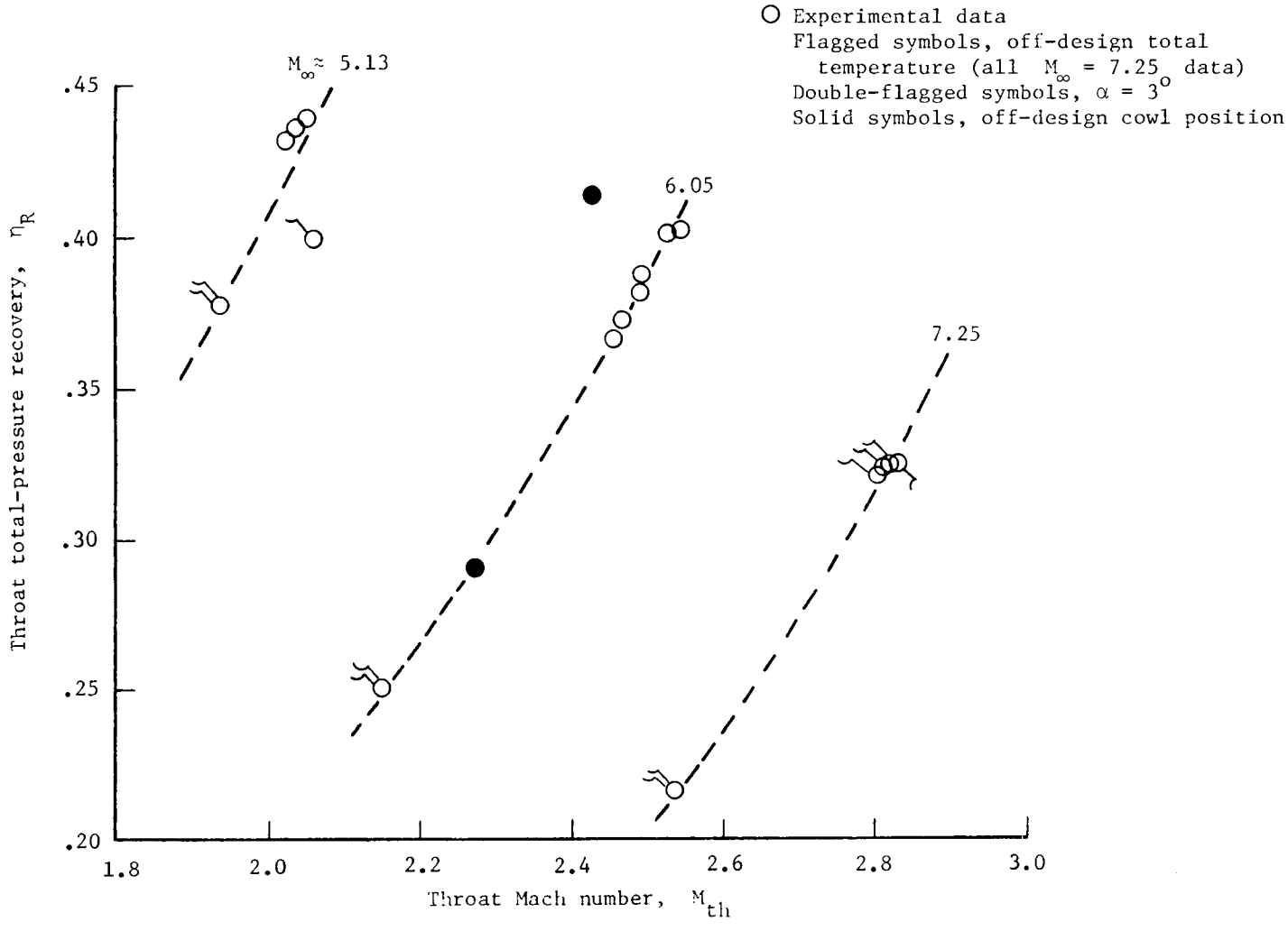

Figure 14.- HRE-AIM total-pressure recovery correlation with throat and free-stream Mach numbers. $\alpha = 0^\circ$ unless otherwise indicated.